

INFRARED SUPERNOVA REMNANTS IN THE SPITZER GLIMPSE FIELD

HO-GYU LEE

Astronomy Program, SEES, Seoul National University, Seoul 151-742, Korea

E-mail: hglee@astro.snu.ac.kr

(Received October 5, 2005; Accepted December 7, 2005)

ABSTRACT

We have searched for infrared emission from supernova remnants (SNRs) included in the Spitzer Galactic Legacy Infrared Mid-Plane Survey Extraordinaire (GLIMPSE) field. At the positions of 100 known SNRs, we made 3.6, 4.5, 5.8, and 8.0 μm band images covering the radio continuum emitting area of each remnant. In-depth examinations of four band images based on the radio continuum images of SNRs result in the identification of sixteen infrared SNRs in the GLIMPSE field. Eight SNRs show distinct infrared emission in nearly all the four bands, and the other eight SNRs are visible in more than one band. We present four band images for all identified SNRs, and RGB-color images for the first eight SNRs. These images are the first high resolution ($<2''$) images with comparative resolution of the radio continuum for SNRs detected in the mid-infrared region. The images typically show filamentary emission along the radio enhanced SNR boundaries. Most SNRs are well identified in the 4.5 and 5.8 μm bands. We give a brief description of the infrared features of the identified SNRs.

Key words : ISM: supernova remnants – infrared

I. INTRODUCTION

Infrared emission from supernova remnants (SNRs) is important in the evolution of SNRs; furthermore, it also delivers unique information pertaining to SNR physics. Dust grains swept up by SNRs are heated and disrupted, and emit infrared radiation that dominate the cooling during most of the SNR lifetime. Their infrared emission contains the most direct informations on the physical processes associated with dust grains behind the SNR shocks (Dwek & Arendt 1992; Draine & McKee 1993). In young SNRs, the thermal infrared emission may reveal the composition of newly condensed dust grains from ejecta, while the non-thermal infrared synchrotron emission is important for understanding the acceleration and evolution of high-energy particles in SNRs. Ionic and H_2 emission lines in infrared emission serve as a very important diagnostic tool for understanding the underlying physics of SNR shocks. This is particularly true for distant SNRs that suffer large extinction. However, despite such usefulness, the infrared is the least-exploited waveband in the study of SNRs.

The all-sky survey by the Infrared Astronomical Satellite (IRAS) detected infrared emission from a significant ($\sim 30\%$) fraction of the known SNRs in the Galaxy (Arendt 1989; Saken et al. 1992). Thus far, the IRAS survey is the only infrared data set that includes the entire ensemble of Galactic SNRs. Although its resolution, of the order of a few-arcminutes, is useful only to the extent that large SNRs do not suffer from any confusion effect, it showed that thermally heated grains are responsible for the far-infrared emission of SNRs. In the mid-infrared region, Kim et al. (2005) reported infrared emission from eight SNRs using the Galactic

plane survey performed by the Midcourse Space Experiment (MSX). The spectral analysis including the IRAS data suggested that the line contribution could be significant in the near/mid infrared. The Infrared Space Observatory (ISO) conducted spectroscopic and imaging observations of nine SNRs covering 3–8 μm bands of of the GLIMPSE field. The majority of them were bright young SNRs such as Cas A, Tycho, Kepler, and Crab (e.g., Douvion et al. 1999, 2001a). Several radiative SNRs interacting with molecular clouds such as IC 443 and 3C 391 show spatially separated molecular and ionic lines (Cesarsky et al. 1999; Reach et al. 2002).

GLIMPSE (Benjamin et al. 2003) is one of the largest surveys performed in the infrared region. The survey provides fully-sampled, confusion-limited 3.6, 4.5, 5.8 and 8.0 μm Spitzer IRAC data for the inner two-thirds region of the Galactic plane with a spatial resolution of $\sim 2''$. Most star formation regions, galactic molecular rings, and more than 4 spiral arms are located in the surveyed area. The GLIMPSE project focuses on Galactic structure and star formation. Concurrently, the wide, deep, and unbiased survey provides a unique opportunity to investigate diffuse objects, which occupy large areas in the sky. In this paper, we studied infrared emission from all SNRs contained in the GLIMPSE Field. Section 2 explains the data and identification method of the infrared emission from individual SNRs. Section 3 reports the identified SNRs and their characteristics. A brief discussion and summary is included in Section 4. An independent study to search for SNRs in the GLIMPSE field (Reach et al. 2005) exists, and we provide a note on their study at the end of this section. Finally, we briefly describe the infrared features of the identified SNRs in the Ap-

pendix.

II. DATA AND IDENTIFICATION OF SNRS

The GLIMPSE data cover two thirds of the inner Galactic plane ($10^\circ < |l| < 65^\circ$, $|b| < 1^\circ$) in four wavelength bands centered at 3.6, 4.5, 5.8, and 8.0 μm (Benjamin et al. 2003). More than 310,000 frames were taken by the Infrared Array Camera (IRAC) across several days between March 9 and November 1, 2004. Each IRAC frame has approximately the same field of view of $5'.2 \times 5'.2$ with a pixel size of $\sim 1''.2$ (Fazio et al. 2004). Their point response function varies within the array. The in-flight mean values of the FWHM are $1''.66$, $1''.72$, $1''.88$, and $1''.98$ in the 3.6, 4.5, 5.8, and 8.0 μm bands, respectively. The total on-source integration time per position was 4 seconds after combining the overlapped and revisited frames. The 5σ sensitivities were estimated as 0.2 mJy for the two shorter bands and 0.4 mJy for the longer two bands. The basic calibration and data handling were performed by the Spitzer Science Center (SSC) Pipeline versions from S9.5.0 to S10.5.0 depending on the observed date. Further image processing, such as column pull-down, banding corrections, masking pixel, and removing stray light, were performed for the image products by the GLIMPSE Pipeline. We used the GLIMPSE Atlas-Mosaicked Images for each band archived by SSC. Each mosaicked image was given by a $1^\circ.1 \times 0^\circ.8$ tile in Galactic coordinates. Among the 231 Galactic SNRs listed in Green's catalog (2004), 100 SNRs exist in the GLIMPSE field. We obtained the images of these 100 SNRs in all the four bands. The images use the equatorial coordinate system and have a pixel size of $1''.2$. For large SNRs or for SNRs spreading across the boundaries of the GLIMPSE Atlas-Mosaicked images, we have coadded adjacent images. The image processing was made by using the SWARP software package distributed by TERAPIX (<http://terapix.iap.fr/soft/swarp>). The imaging centers were adopted from Green's catalog, and the sizes were chosen to cover areas larger than their respective radio continuum extents: $12'$ for SNRs smaller than $8'$, $30'$ for those between $9'$ and $20'$, and $60'$ for those larger than $21'$.

The identification of SNRs requires careful inspection because they usually appear as faint filaments embedded in a complex field with confusing sources such as H II regions and planetary nebulae. For each SNR, we examined all four band images simultaneously to search for infrared features coincident with the radio continuum emission. Two radio continuum data sets were used for the comparison, i.e., NRAO* VLA Sky Survey (Condon et al. 1998) for the northern SNRs and

the MOST[†] Supernova Remnant Catalog (Whiteoak & Green 1996) for the southern SNRs. The identified SNRs were compared in detail with high-resolution radio continuum images for confirmation.

III. RESULTS

Among the 100 SNRs examined, eight bright SNRs are distinctly identified. They are listed in Table 1. The position, size, and type in columns (2)–(5) are quoted from the Green's catalog. These SNRs show infrared emission in all four bands at the peak position, and the extent of the emission is comparable to the remnant size. Figures 1 to 8 show their images. The gray-scale range varies from the median of the image pixels to three times of their standard deviations. This, however, does not hold in the case of two SNRs, which show a variation of up to five times for W 49B and seven times for G349.7+0.2. In each figure, a radio continuum map is also included at the bottom left to assist in the verification of the associated infrared emission features. The position and scale of radio continuum maps are set to match those of the infrared images. The radio continuum maps have angular resolutions of $2''$ – $5''$ except several SNRs in the southern sky and the large SNR W 44. Thus, in most cases, thin filamentary features in the infrared can be directly compared to the corresponding features in radio. Figures 9 to 16 show RGB-color images of these SNRs created from 8.0 μm (Red), 5.8 μm (Green), and 4.5 μm (Blue) images. The dynamic range of each color is identical to its gray-scale image.

In addition to the above eight SNRs, we have identified another eight SNRs that are marginally bright enough to be discernible from the background. They are also listed in Table 1, and their images are shown in Figures 17 to 24. The scale range of the figures are narrower than (typically half of) those for the distinctly-identified SNRs to show the associated emission more clearly. All these SNRs are identified in the 4.5 and 5.8 μm bands except G54.1+0.3, which is identified only in the 8.0 μm band. G11.2–0.3 and 3C 396 are also visible in the 8.0 μm band. G298.6–0.0 has a bright filament visible in all four bands; however, its association is questionable.

The GLIMPSE images show that the infrared emission of SNRs usually appear as partial filaments or almost complete thin shells along the SNR boundary. Kes 17, G311.5–0.3, and RCW 103 are good examples. All marginally-identified SNRs except G54.1+0.3 belong to this category. In W 44 and W 49B, the filaments are also seen inside the remnants, which might be located on the shell in a projected manner. The partial filaments are found typically at the positions of enhanced radio emission and are aligned along the

*The National Radio Astronomy Observatory is a facility of the National Science Foundation operated under cooperative agreement by Associated Universities, Inc.

[†]The MOST is operated by the University of Sydney with support from the Australian Research Council and the Science Foundation for Physics within the University of Sydney.

Table 1. SNRs Identified in the Spitzer GLIMPSE field

Name	RA ^a	Dec ^a	Size ^a	Type ^a	IRAS Flux ^b (Jy)				IRAC Morphology
	(h m s)	(^o ′)	(′ × ′)		12	25	60	100	
Distinctly identified SNRs									
G31.9+0.0 (3C391)	18 49 25	−00 55	7×5	S	3 (2)	14 (7)	180 (90)	160 (80)	Thick shell broken-out toward southeast
G34.7−0.4 (W44)	18 56 00	+01 22	35×27	C	410 (100)	440 (110)	4400 (1100)	13000 (6500)	Bright thin filaments inside the entire remnant
G43.3−0.2 (W49B)	19 11 08	+09 06	4×3	S	15 (3)	140 (28)	1100 (220)	2000 (400)	Bright thin filaments inside the entire remnant
G304.6+0.1 (Kes 17)	13 05 59	−62 42	8	S	17 (12)	24 (17)	160 (110)	440 (310)	Bright thin filaments along the western shell
G311.5−0.3	14 05 38	−61 58	5	S	<4	<12	<190	<310	Almost complete thin filamentary ring
G332.4−0.4 (RCW 103)	16 17 33	−51 02	10	S	<200	<260	<3000	<5400	Bright thin filament along the southern shell
G348.5+0.1 (CTB 37A)	17 14 06	−38 32	15	S	<150	<250	<2500	<8000	Thick shell broken-out toward southwest
G349.7+0.2	17 17 59	−37 26	2.5×2	S	12 (4)	48 (16)	370 (120)	<550	Very bright filament with bright spot at center
Marginally identified SNRs									
G11.2−0.3	18 11 27	−19 25	4	C	44 (4)	189 (19)	1400 (140)	3100 (310)	Thin partial filament at the radio-bright portion of southeastern shell
G21.8−0.6 (Kes 69)	18 32 45	−10 08	20	S	106 (16)	121 (18)	1370 (210)	6300 (950)	Thin filament at the middle of radio shell
G39.2−0.3 (3C396)	19 04 08	+05 28	8×6	C	<56	<82	<530	<960	Filamentary emission spread over the western part of remnant
G41.1−0.3 (3C397)	19 07 34	+07 08	4.5×2.5	S	<12	<23	<224	<485	Very faint filament at the radio enhanced portion of northeastern shell
G54.1+0.3	19 30 31	+18 52	1.5	F?	<21	18 (6)	26 (9)	<600	Diffuse emission at western boundary with extended tail toward north
G298.6−0.0	12 13 41	−62 37	12×9	S	<110	<230	<1940	<3650	Bright but suspected filament along southern shell
G340.6+0.3	16 47 41	−44 34	6	S	<23	<32	<370	<1100	Thin filament at south overlapped with unrelated confusing emission
G346.6−0.2	17 10 19	−40 11	8	S	<160	<180	<1500	<5900	Thin filament at south overlapped with unrelated confusing emission

^aReferred from the Green's catalog (2004).^bThe first row is the measured flux and the second row in parentheses is the uncertainty of measuring flux (Arendt 1989).

radio shell. However, the coincidence decreases for the detailed structures. For example, the radio-bright western shell has no infrared counterpart in W 44. In addition, with regard to the fields under investigation, all the radio-bright SNRs do not have associated infrared emission. Two SNRs, - 3C 391 and CTB 37A - have rather thick shells, and they appear to have broken-out shell morphology like radio features. G349.7+0.2 is unique on account of its very bright infrared emission in the central area of the remnant. This remnant is interacting with a molecular cloud at the center (Lazendic et al. 2005), and the infrared-bright region coincides with the position of the molecular cloud. For each SNR, we give a brief description of their infrared features in the Appendix.

The infrared emission of SNRs are better identified in the 4.5 and 5.8 μm bands than in the other two bands. In the 3.6 μm band, the infrared emission from the SNRs is weak. Concurrently, the emission from stars makes it difficult to identify the SNR emission. On the other hand, the 8.0 μm band is severely affected by Polycyclic Aromatic Hydrocarbon (PAH) emission at 6.2, 7.7, and 8.6 μm , which is dominant in H II regions, planetary nebulae, and other diffuse Photodissociation Regions (PDRs) (van Dishoeck 2004). Therefore, the emission from SNRs is easily confused with those from other sources. Hence, most of the identified SNRs show blue (4.5 μm) or green filaments (5.8 μm) in the RGB images.

IV. DISCUSSION AND SUMMARY

We have identified 16 (8 distinctly and 8 marginally) infrared SNRs in the GLIMPSE field. This is 16% of the 100 radio/X-ray SNRs in the field. For comparison, previous IRAS studies detected infrared emissions from 22 SNRs out of the 70 (Arendt 1989) or 18 SNRs out of the 75 (Saken et al. 1992), which were identified in the GLIMPSE field at the time of the respective studies. Among the 16 GLIMPSE SNRs, 9 SNRs are detected by IRAS. IRAS fluxes or limits are listed in columns (6)–(9) of Table 1. A study was conducted to search for the infrared emission associated with SNRs from the Midcourse Space Experiment (MSX) data (Kim et al. 2005). MSX surveyed the whole Galactic plane ($|b| < 5^\circ$) in four bands centered at 8.28, 12.13, 14.65, and 21.34 μm . Kim et al. (2005) generated and examined the MSX images of over 200 SNRs in the field and identified 8 SNRs, five of which are included in the GLIMPSE field. These five SNRs, - G11.2–0.3, W 44, W 49B, G54.1+0.3, and G349.7+0.2 - are identified in this work. The higher detection rate of the GLIMPSE survey is due to its higher sensitivity and angular resolution. The 0.4 mJy sensitivity of the 8 μm band in the GLIMPSE field is seven times better than the 30 mJy sensitivity of the 8.28 μm band of MSX (Benjamin et al. 2003). Furthermore, the $18''.3$ resolution of MSX increases the chance to dilute thin filaments and confuse them with other sources. An-

other large-scale IR survey is the Two Micron All Sky Survey (2MASS), which surveyed the whole sky at J (1.25 μm), H (1.65 μm), and K_s (2.17 μm). No systematic study of SNRs using the 2MASS data exists; however, four SNRs (Crab, IC 443, Cas A, and RCW 103) have been reported as visible. Only RCW 103 exists in the GLIMPSE field. We checked 2MASS images at the position of the other GLIMPSE SNRs and were barely able to trace the emission associated with W 49B and W 44.

In general, the infrared emission from SNRs is composed of a thermal continuum from shock-heated dust grains, line emission from shock-heated gas, and synchrotron emission. Among the 16 GLIMPSE SNRs, only one is Crab-like (or filled-center) and three are composite with a central pulsar wind nebulae (PWNe) (see Table 1). We have not detected any IR emission corresponding to these synchrotron nebulae. Except G54.1+0.3, all the 16 SNRs show shell-like or filamentary IR emission. If we consider the steep slope of the synchrotron emission and the low sensitivity of the GLIMPSE data, it is highly unlikely that the synchrotron emission contributes to the observed IR flux even in the shortest IRAC wave band (3.6 μm). On the other hand, previous ISO spectroscopic studies of SNRs showed that ionic lines [Fe II] 5.340 μm and [Ar II] 6.985 μm in the IRAC bands are particularly strong in radiative shocks (Arendt 1999; Oliva et al. 1999; Douvion et al. 1999, 2001a, 2001b; Reach et al. 2002). For SNRs interacting with molecular clouds, e.g., 3C 391 and IC 443, shock-excited H_2 lines are also found to be strong (Cesarsky et al. 1999; Reach & Rho 2000; Reach et al. 2002). Therefore the ionic lines produced by the atomic J-type shock (Hartigan et al. 2004) and/or the H_2 lines produced by the molecular C-type shock (Hollenbach et al. 1989) can be the main contributors in IRAC images.

Independent of this work, there exists a study on the search for SNRs in the GLIMPSE field (Reach et al. 2005). They also detected the associated infrared emission by visually inspecting the IRAC images with an overlaid radio map. 18 SNRs were reported to have an associated infrared emission (score 1). All eight distinct SNRs, as well as the five of the eight marginally detected SNRs were included in their list. The others (G54.1+0.3, G298.6–0.0, G340.6+0.3) were regarded as SNRs that were not convincingly detected due to the confusion with unrelated emissions. For the detected SNRs, the origin of the infrared emission, e.g., molecular or ionic shocks or the PAH emission, was discussed using the relative intensities between the IRAC bands.

The GLIMPSE images of SNRs presented in this paper are the first high-resolution infrared images for most SNRs. They show that SNRs appear as almost complete shells, partial filaments, or a combination of filaments. The infrared emission generally coincides with the radio continuum, e.g., the infrared emission is identified with the radio-bright regions, although some displacement is a feature of the detailed distribution.

Most are relatively well identified in the 4.5 and 5.8 μm bands. The dominant contribution may originate from the line emission of shocked ambient gas. We expect that the infrared imaging and spectroscopic observations using the SST and the future ASTRO-F mission will extend the understanding of the nature of the infrared emission in individual sources.

ACKNOWLEDGEMENTS

This work is based on archival data obtained with the Spitzer Space Telescope, which is operated by the Jet Propulsion Laboratory, California Institute of Technology under a contract with NASA. I wish to thank the Spitzer GLIMPSE team for their efforts. This work was supported by the Korea Science and Engineering Foundation Grant ABRL 3345-20031017. I wish to thank the Institute of Space and Astronautical Science (ISAS) for providing their facilities during part of this work. I wish to thank Bon-Chul Koo for extensive advice on the entire study. I also wish to thank David Moffett, Stephen Reynolds, Kristy Dyer, David Green, John Dickel, and Crystal Brogan for providing the high-resolution radio continuum images, and Chris Pearson for the advice to improve the presentation.

REFERENCES

- Arendt, R. G., 1989, *ApJS*, 70, 181
- Arendt, R. G., Dwek, E., & Moseley, S. H. 1999, *ApJ*, 521, 234
- Benjamin, R. A., et al., 2003, *PASP*, 115, 953
- Brogan, C. L., Frail, D. A., Goss, W. M., & Troland, T. H., 2000, *ApJ*, 537, 875
- Cesarsky, D., Cox, P., Pineau des Forêts, G., van Dishoeck, E. F., Boulanger, F., & Wright, C. M., 1999, *A&A*, 348, 945
- Condon, J. J., Cotton, W. D., Greisen, E. W., Yin, Q. F., Perley, R. A., Taylor, G. B., & Broderick, J. J., 1998, *AJ*, 115, 1693
- Dickel, J. R., Green, A., Ye, T., & Milne, D. K., 1996, *AJ*, 111, 340
- Douvion, T., Lagage, P. O., & Cesarsky, C. J., 1999, *A&A*, 352, L111
- Douvion, T., Lagage, P. O., & Pantin, E., 2001a, *A&A*, 369, 589
- Douvion, T., Lagage, P. O., Cesarsky, C. J., & Dwek, E., 2001b, *A&A*, 373, 281
- Draine, B. T., & McKee, C. F., 1993, *ARAA*, 31, 373
- Dwek, E., 1987, *ApJ*, 322, 812
- Dwek, E., & Arendt, R. G., 1992, *ARAA*, 30, 11
- Dyer, K. K. & Reynolds, S. P., 1999a, *ApJ*, 526, 365
- Dyer, K. K. & Reynolds, S. P., 1999b, *BAAS*, 31, 9735
- Fazio, G. G. et al., 2004, *ApJS*, 154, 10

- Green, D. A., Gull, S. F., Tan, S. M., & Simon, A. J. B., 1988, *MNRAS*, 231, 735
- Green, D. A., 2004, *Bulletin of the Astronomical Society of India*, 32, 335–370.
- Hartigan, P., Raymond, J., & Pierson, R., 2004, *ApJL*, 614, L69
- Hollenbach D. J., Chernoff, D. F., & McKee, C. F., 1989, In *Infrared Spectroscopy in Astronomy*, ESA SP-290, pp. 245–58, Noordwijk, ESTEC
- Kim et al., 2005, in preparation
- Lazendic, J. S., Slane, P. O., Hughes, J. P., Chen, Y., & Dame, T. M., 2005, *ApJ*, 618, 733
- Moffett, D. A. & Reynolds, S. P., 1994, *ApJ*, 425, 668
- Oliva, E., Moorwood, A. F. M., Drapatz, S., Lutz, D., & Sturm, E., 1999, *A&A*, 343, 943
- Reach, W. T. & Rho, J., 1999, *ApJ*, 511, 836
- Reach, W. T. & Rho, J., 2000, *ApJ*, 544, 843
- Reach, W. T., Rho, J., & Jarrett, T. H., 2002, *ApJ*, 564, 302
- Reach, W. T. et al., 2005, *AJ*, in press
- Saken, J. M., Fesen, R. A., & Shull, J. M., 1992, *ApJS*, 81, 715
- van Dishoeck, E. F., 2004, *ARAA*, 42, 119
- Whiteoak, J. B. Z. & Green, A. J., 1996, *A&AS*, 118, 329 (on-line version at <http://www.physics.usyd.edu.au/astrop/wg96cat>)

APPENDIX. IDENTIFIED SNRS

G11.2–0.3 – A faint wispy filament is seen along the SE SNR boundary at 4.5, 5.8, and 8.0 μm . The $\sim 20''$ -long filament centered at ($18^{\text{h}}11^{\text{m}}31^{\text{s}}.7, -19^{\circ}27'14''$) is particularly noticeable. The bright emission at ($18^{\text{h}}11^{\text{m}}19^{\text{s}}.3, -19^{\circ}26'19''$) is not associated with the remnant but with a K1/K2 III star (HD 166422).

G21.8–0.6 (Kes 69) – A faint $\sim 6'$ -long filament centered at ($18^{\text{h}}33^{\text{m}}05^{\text{s}}.9, -10^{\circ}12'53''$) is seen along the incomplete SNR shell at 4.5 and 5.8 μm . There is a complex, extended emission at 5.8 and 8.0 μm in the NE boundary of the field. The SE boundary of this structure appears to form a concave filament that is roughly parallel with the SNR radio shell. The relation of this emission to the remnant needs to be explored.

G31.9+0.0 (3C391) – A bright incomplete shell coincident with the radio structure is seen. The NW part of the remnant is bright primarily at 5.8 μm , while the NE and SW parts are bright at 4.5, 5.8, and 8.0 μm ; this explains their different colors in the true-color image. The bright region at ($18^{\text{h}}49^{\text{m}}23^{\text{s}}.3, -00^{\circ}57'49''$) shows

a region where the remnant interacts with a molecular clump (Reach & Rho 1999).

G34.7+0.4 (W44) – A bright filamentary elliptical shell coincident with the radio shell is seen in all the four bands. It is most clearly seen at $4.5\ \mu\text{m}$, which yields a blue color in the true-color image. The eastern edge of the infrared shell is missing although it is bright in the radio image.

G39.2–0.3 (3C396) – A faint $\sim 2'$ -long filament is seen along the SW SNR boundary where the radio emission is enhanced. It is most clearly visible at $4.5\ \mu\text{m}$. The emission at ($19^{\text{h}}03^{\text{m}}56^{\text{s}}.2, +05^{\circ}25'43''$) is also be identified in other bands.

G41.1–0.3 (3C397) – Very faint filaments coincident with the NE SNR boundary are visible at 4.5, 5.8, and $8.0\ \mu\text{m}$. The identified filaments are partly affected by the emission from a bright confusing star located at ($19^{\text{h}}07^{\text{m}}33^{\text{s}}.6, +07^{\circ}09'24''$).

G43.3–0.2 (W49B) – A bright filamentary shell matching the radio structure is seen in all the four bands. The SW portion of the shell is very bright as it is in the radio. The interior of the remnant is filled with diffuse emission including several bright filaments running along the NE-SW direction. A bow-shaped structure bright at $8.0\ \mu\text{m}$ exists just outside the eastern boundary of the remnant; its association needs to be explored.

G54.1+0.3 – A partially complete, circular shell is seen mainly at $8.0\ \mu\text{m}$. The western half of the shell is bright and thick, whereas the eastern half is faint and fuzzy. The remnant is Crab-like in the radio and the shell appears to surround the remnant. In addition, a diffuse, extended emission emanate from the north of the remnant.

G298.6–0.0 – A $\sim 5'$ -long filament coincident with the southern, radio-bright SNR shell is seen in all the four bands. However, the remnant is located in a complex field, and the possibility of a chance coincidence cannot be ruled out.

G304.6+0.1 (Kes 17) – Bright filaments are distinct in all the four bands. They are distributed in the western part of the remnant along its boundary. At 5.8 and $8.0\ \mu\text{m}$, the filaments appear to be connected to the edge of a large cloud in the NE by a diffuse, extended emission. No infrared counterpart is detected at the south of the remnant where the radio emission is stronger than the western shell.

G311.5–0.3 – An almost complete thin shell with a diameter of $\sim 3'$ is seen in all the four bands. It is brightest at 4.5 and $5.8\ \mu\text{m}$. The western part of the shell is brighter than the eastern part.

G332.4–0.4 (RCW 103) – A sharp filament corresponding to the southern part of the remnant is visible in all the four bands. It is particularly bright at $4.5\ \mu\text{m}$. The bright portion of the filament is at the position where the radio brightness has a sharp cutoff in contrast to the other parts of the remnant. There is also a faint infrared filament corresponding to the western radio-bright region.

G340.6+0.3 – A complex filamentary structure superposed on the northern part of the remnant is visible at 5.8 and $8.0\ \mu\text{m}$. However, it is not correlated with the radio structure of the remnant, and its association needs to be explored. Some diffuse emission coincident with the southern SNR shell also exists.

G346.6–0.2 – A very faint thin filament delineating the SE boundary of the SNR shell is visible at 4.5 and $5.8\ \mu\text{m}$. There exists some faint emission coincident with the northern SNR shell; however, its association is not clear because of the confusing extended structure to the west of the remnant.

G348.5+0.1 – A large ($\sim 10'$) incomplete shell is seen mainly at 5.8 and $8.0\ \mu\text{m}$. The remnant is composed of a small, bright NE portion and a large, diffuse SW portion in the radio, and the infrared shell coincides with the SW portion. The infrared shell is brighter toward the NE where the radio structure starts to blow out. The remnant appears to be connected to a diffuse, extended structure at the NE.

G349.7+0.2 – Bright filamentary emission is visible in the interior of the remnant in all the four bands. A very bright $\sim 40''$ -long, "v"-shaped filament at the center and a bright $\sim 45''$ -long filament perpendicular to the former in the south are prominent. These filaments coincide with the position of the molecular clouds swept up by the SNR shock (Lazendic et al. 2005). Another bright filament stemming out from the eastern end of the "v"-shaped filament is visible along the NE SNR shell. A long filamentary emission is connected to the south of the remnant at 5.8 and $8.0\ \mu\text{m}$. This emission stretches out $\sim 3'$ toward the east.

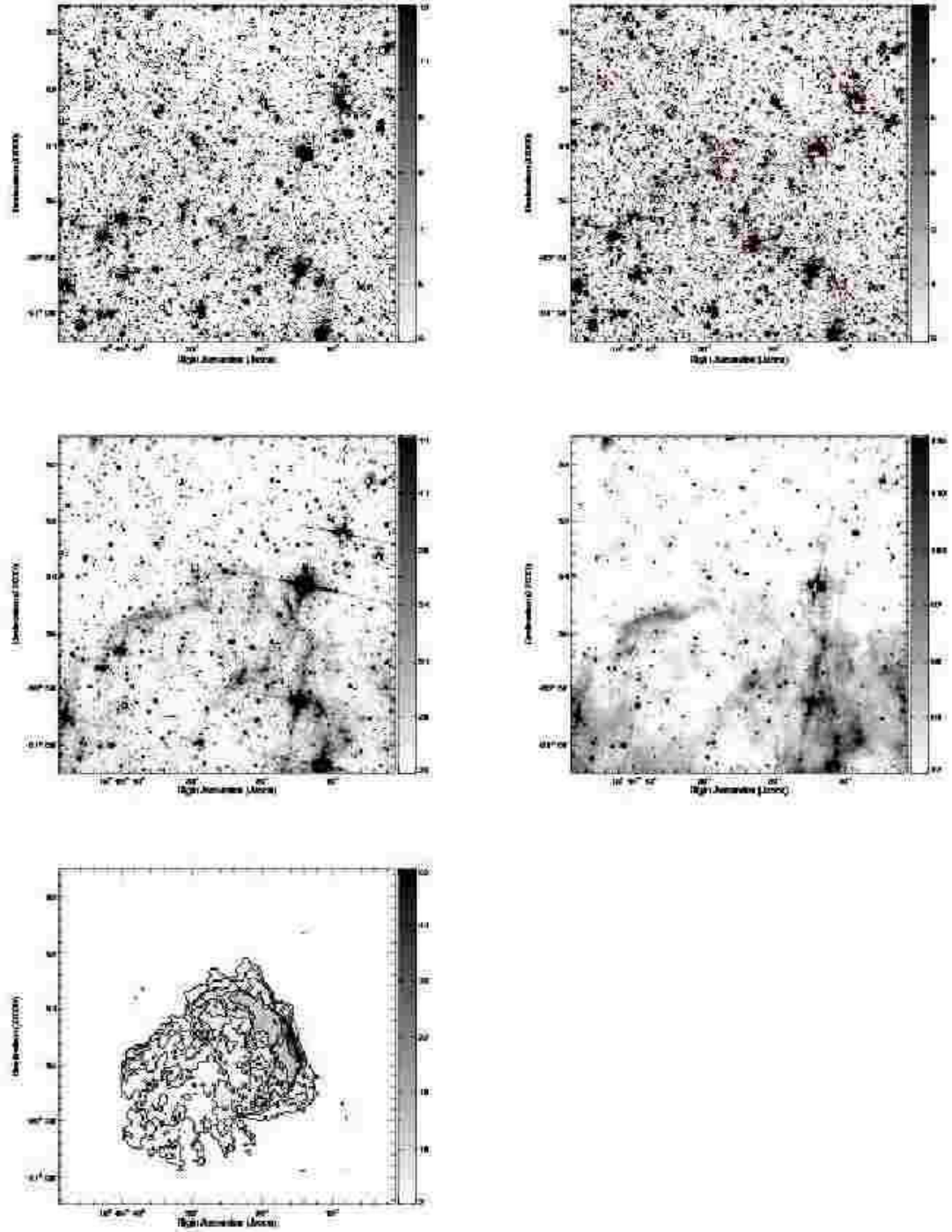


Fig. 1.— IRAC images of G31.9+0.0 (3C 391) at 3.6 μm (top-left), 4.5 μm (top-right), 5.8 μm (middle-left), and 8.0 μm (middle-right). The gray-scale range is shown at the left of each image. VLA 1.46 GHz continuum image with $5''.0 \times 4''.6$ beam (Moffett & Reynolds 1994) is also shown at the bottom-left. The contour levels are 1, 2.5, 5, 7.5, 10, 20, and 40 mJy beam^{-1} .

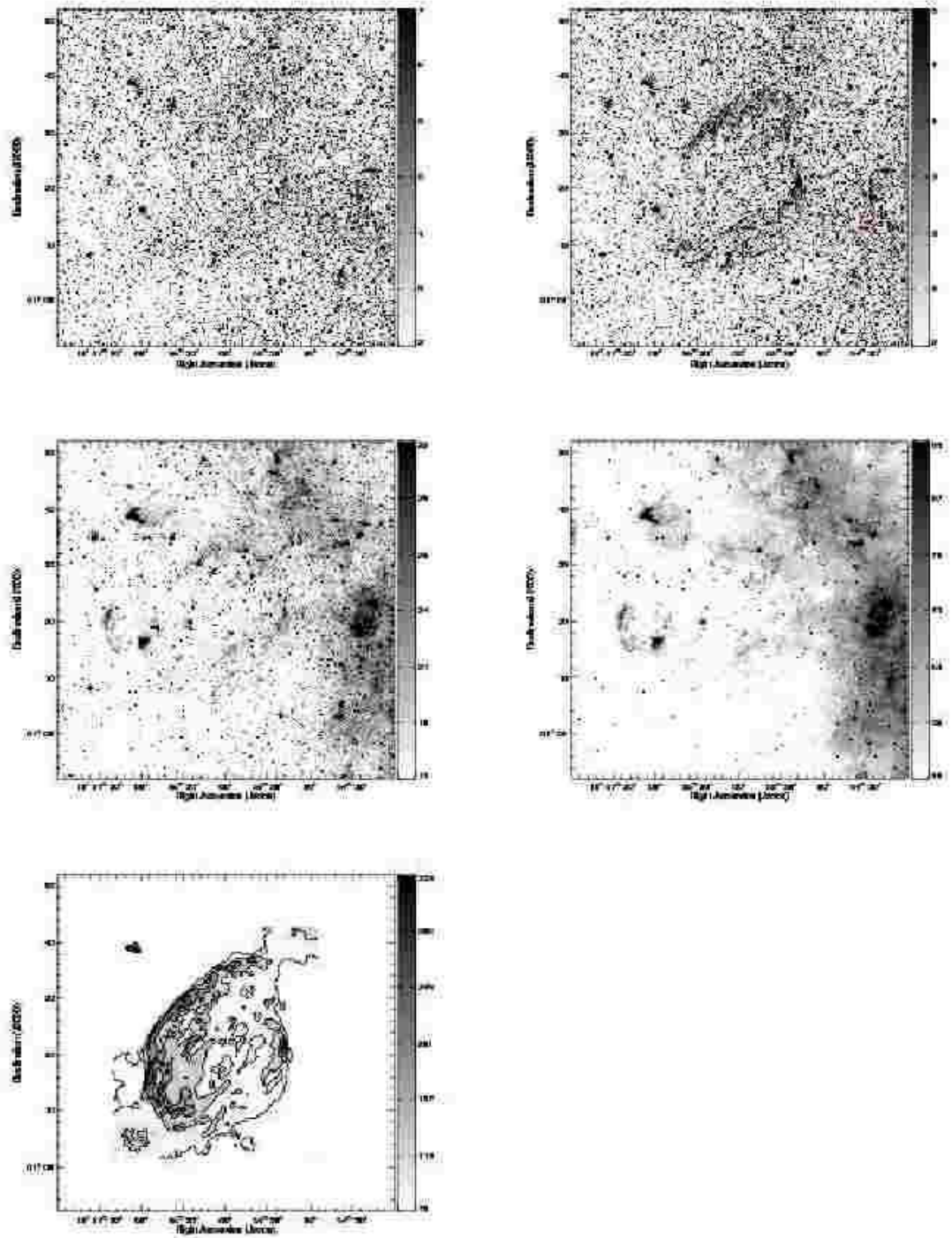


Fig. 2.— IRAC images of G34.7-0.4 (W 44) at 3.6 μm (top-left), 4.5 μm (top-right), 5.8 μm (middle-left), and 8.0 μm (middle-right). The gray-scale range is shown at the left of each image. VLA 1.44 GHz continuum image with $30''.0 \times 30''.0$ beam is also shown at the bottom-left. The contour levels are 50, 100, 150, and 200 mJy beam $^{-1}$.

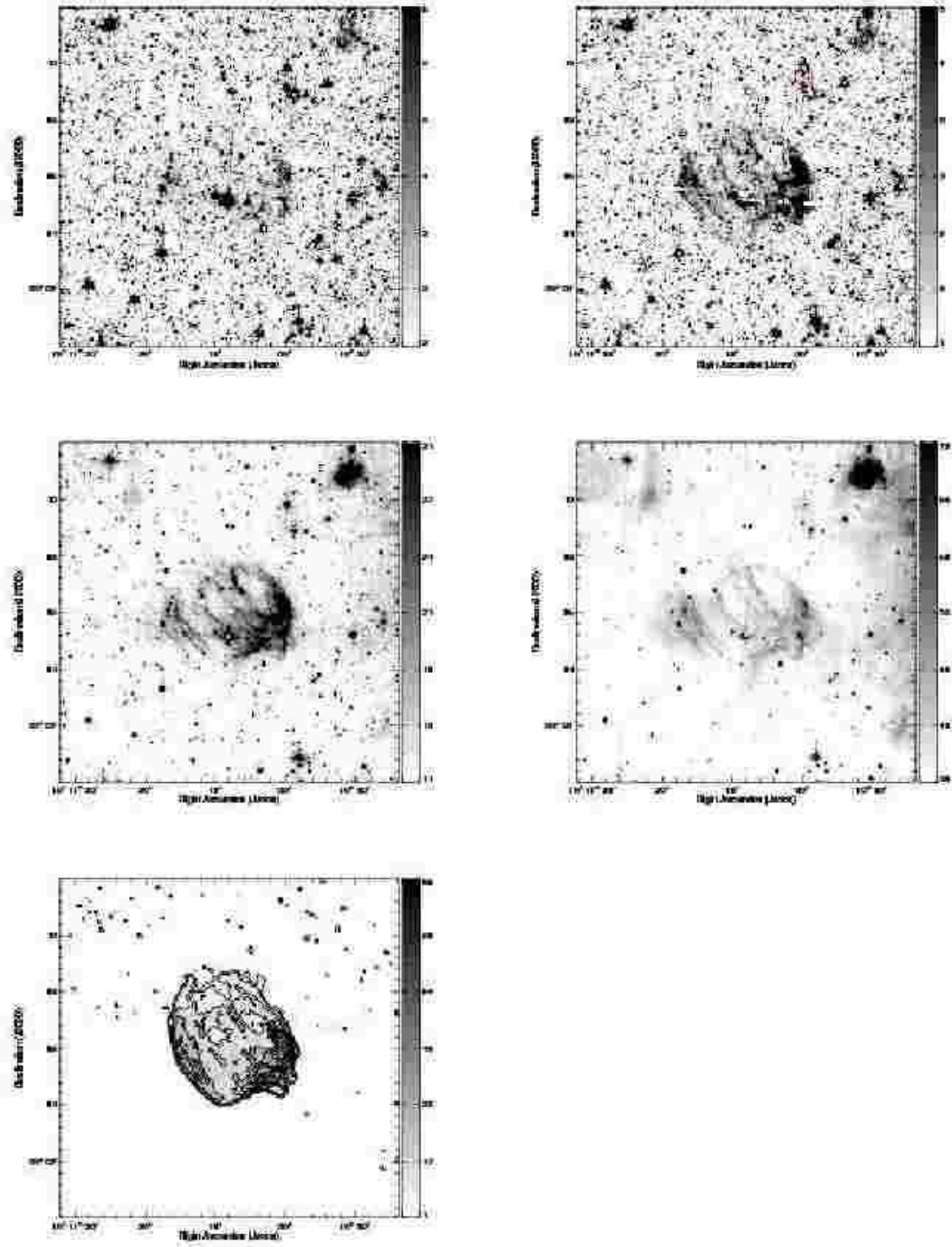


Fig. 3.— IRAC images of G43.3–0.2 (W 49B) at $3.6\ \mu\text{m}$ (top-left), $4.5\ \mu\text{m}$ (top-right), $5.8\ \mu\text{m}$ (middle-left), and $8.0\ \mu\text{m}$ (middle-right). The gray-scale range is shown at the left of each image. VLA 1.45 GHz continuum image with $5''.2 \times 4''.8$ beam (Moffett & Reynolds 1994) is also shown at the bottom-left. The contour levels are 3, 5, 10, 20, 30, 40, and 50 mJy beam $^{-1}$.

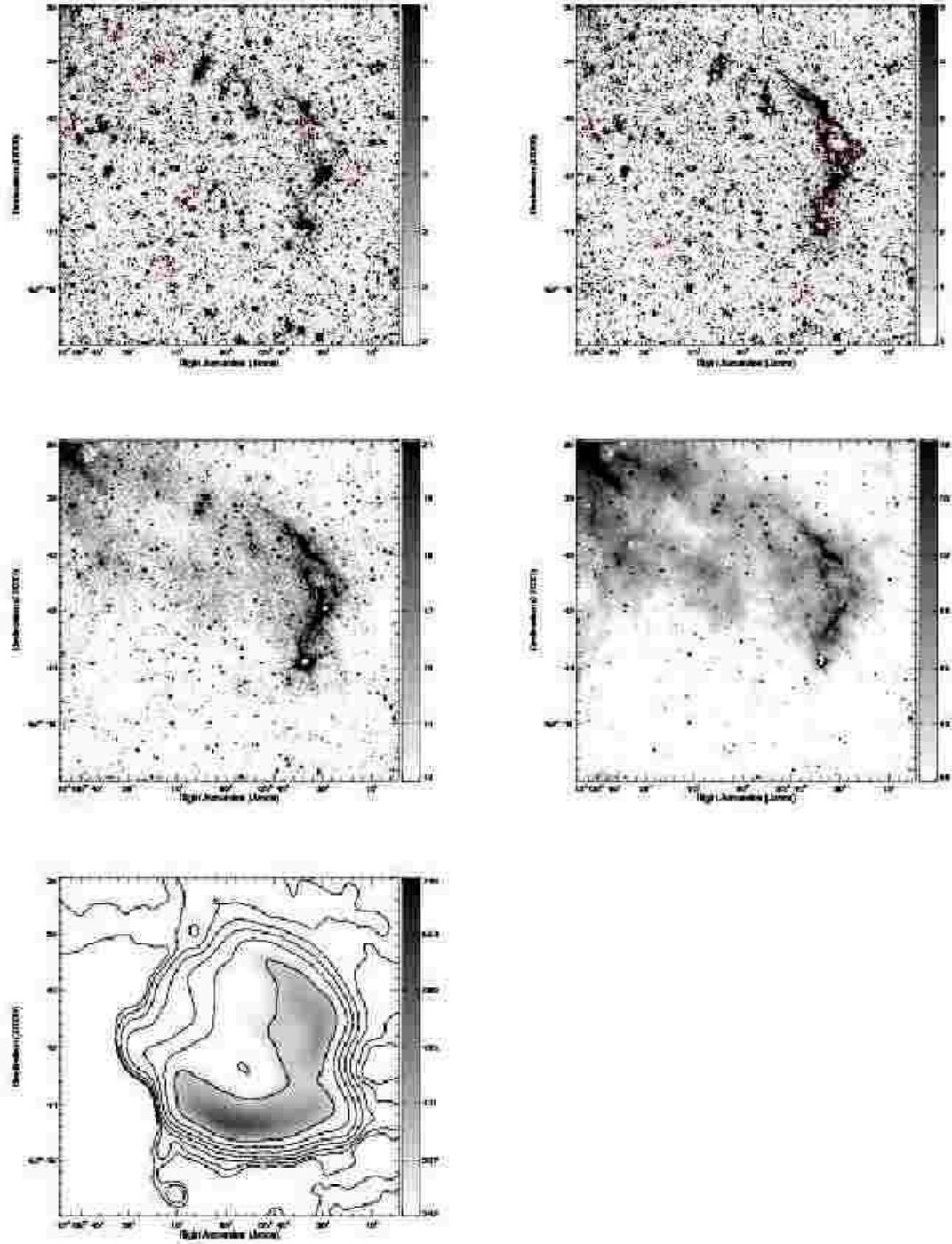


Fig. 4.— IRAC images of G304.6+0.1 (Kes 17) at 3.6 μm (top-left), 4.5 μm (top-right), 5.8 μm (middle-left), and 8.0 μm (middle-right). The gray-scale range is shown at the left of each image. MOST 0.843 GHz continuum image with $43'' \times 43''$ beam is also shown at the bottom-left. The contour levels are 5, 10, 20, 40, 80, 160, and 320 mJy beam^{-1} .

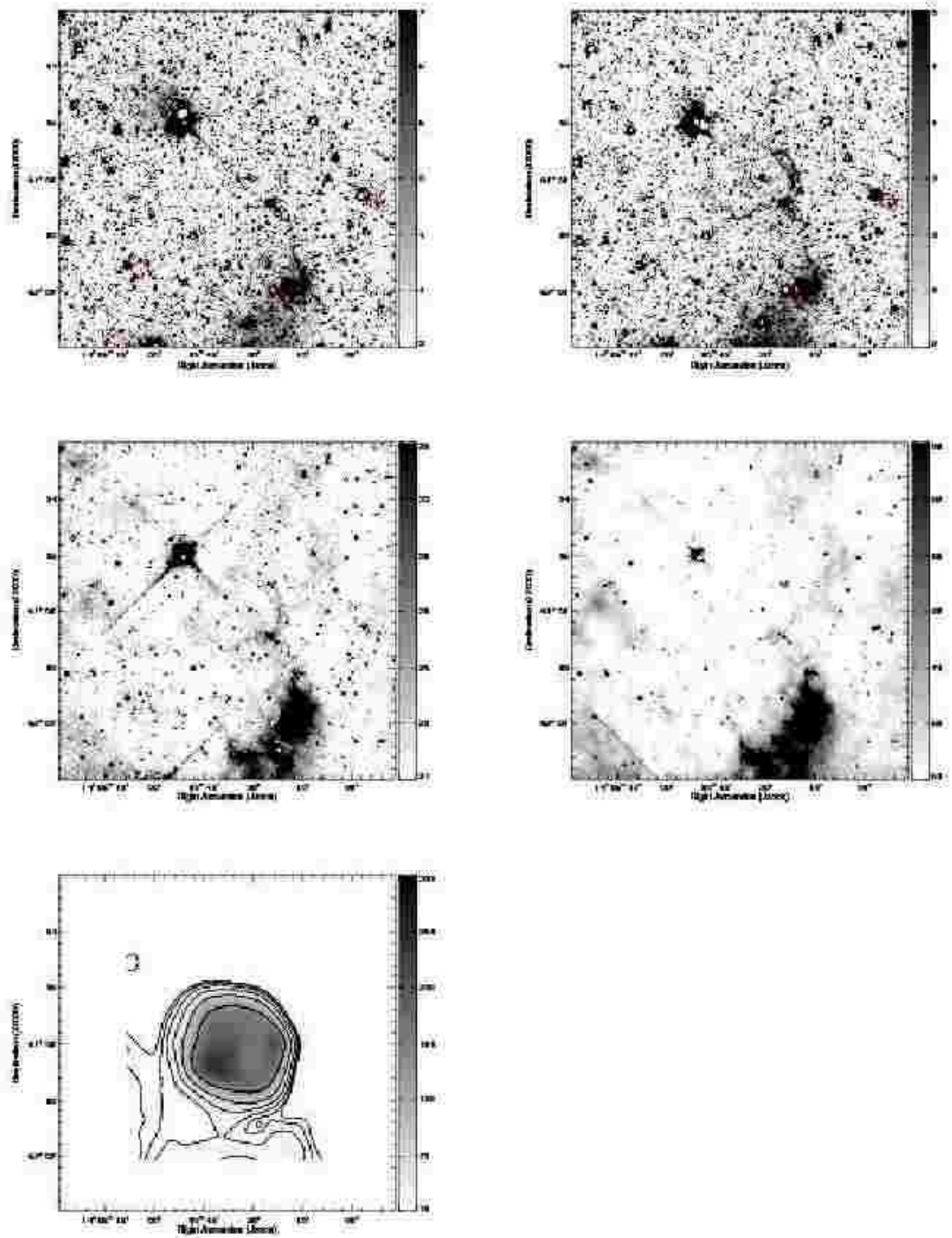


Fig. 5.— IRAC images of G311.5–0.3 at 3.6 μm (top-left), 4.5 μm (top-right), 5.8 μm (middle-left), and 8.0 μm (middle-right). The gray-scale range is shown at the left of each image. MOST 0.843 GHz continuum image with $43'' \times 43''$ beam is also shown at the bottom-left. The contour levels are 5, 10, 20, 40, 80, and 160 mJy beam $^{-1}$.

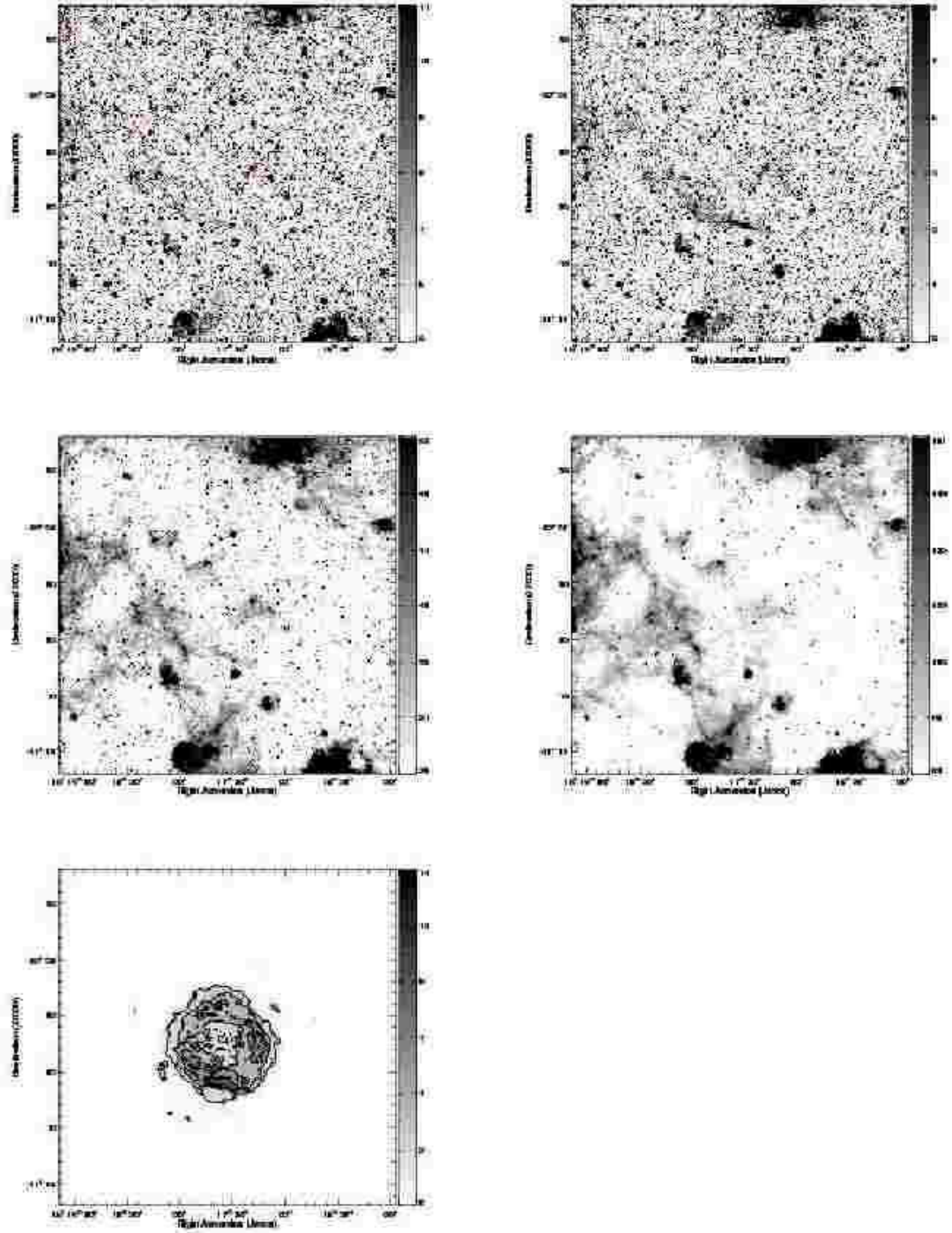


Fig. 6.— IRAC images of G332.4-0.4 (RCW 103) at 3.6 μm (top-left), 4.5 μm (top-right), 5.8 μm (middle-left), and 8.0 μm (middle-right). The gray-scale range is shown at the left of each image. ATCA 2.32 GHz continuum image with $4''.4 \times 3''.7$ beam (Dickel et al. 1996) is also shown at the bottom-left. The contour levels are 1, 3, 5, and 7 mJy beam $^{-1}$.

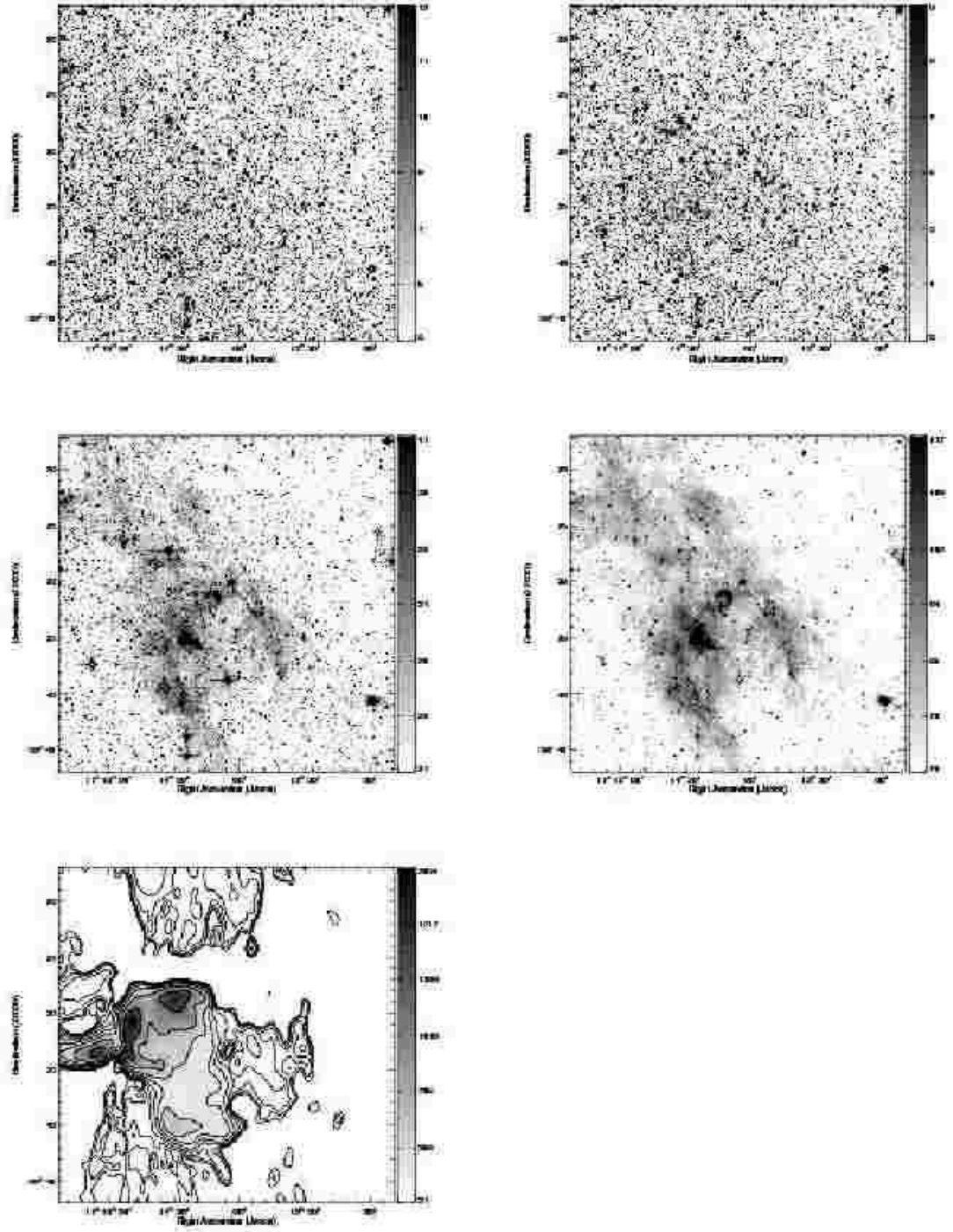


Fig. 7.— IRAC images of G348.5+0.1 (CTB 37A) at 3.6 μm (top-left), 4.5 μm (top-right), 5.8 μm (middle-left), and 8.0 μm (middle-right). The gray-scale range is shown at the left of each image. MOST 0.843 GHz continuum image with $43'' \times 43''$ beam is also shown at the bottom-left. The contour levels are 5, 10, 20, 40, 80, 160, 320, 640, and 1280 mJy beam^{-1} .

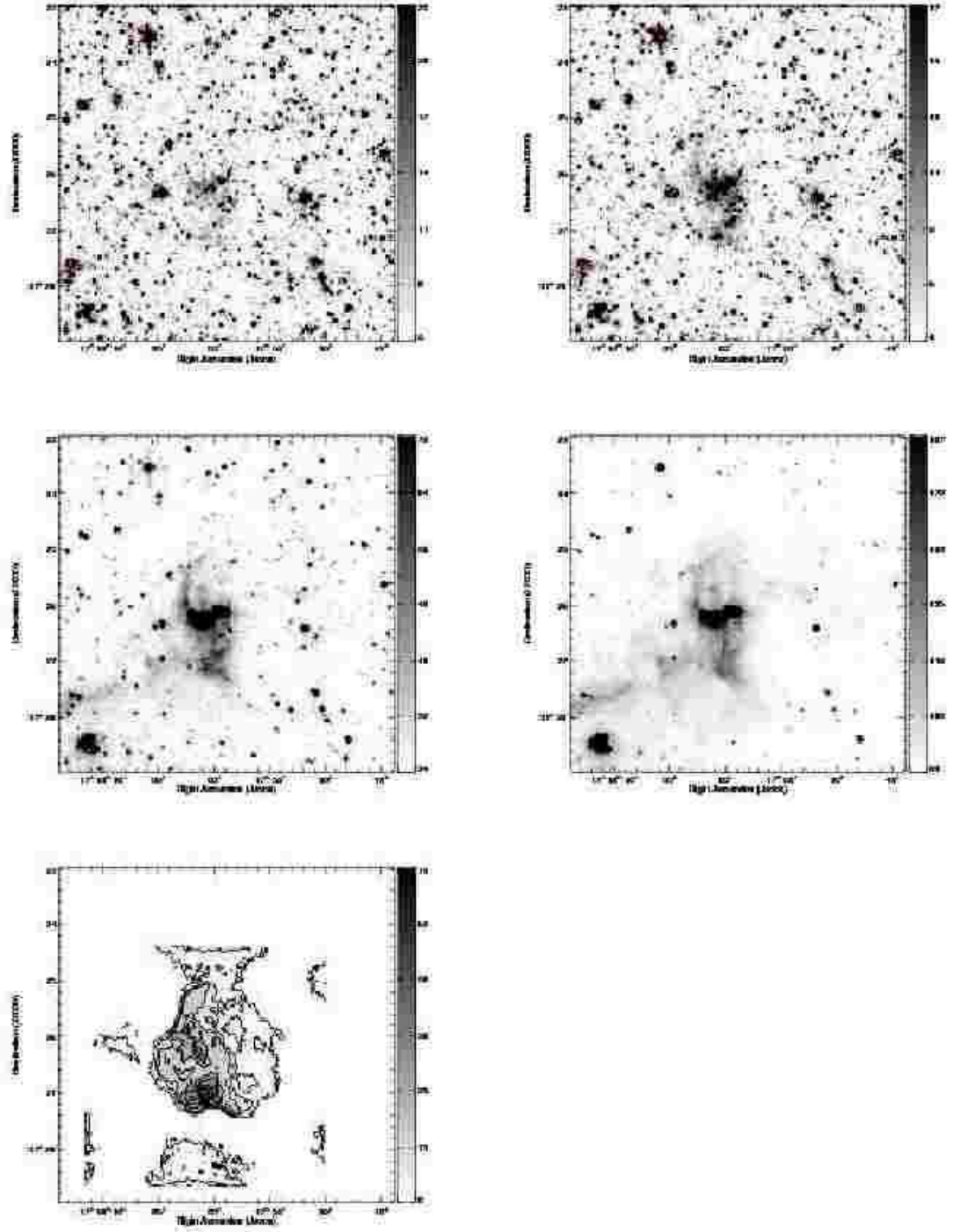


Fig. 8.— IRAC images of G349.7+0.2 at 3.6 μm (top-left), 4.5 μm (top-right), 5.8 μm (middle-left), and 8.0 μm (middle-right). The gray-scale range is shown at the left of each image. VLA 1.51 GHz continuum image with $5''.0 \times 2''.1$ beam (Brogan et al. 2000) is also shown at the bottom-left. The contour levels are 1, 5, 10, 20, 30, 40, and 50 mJy beam $^{-1}$.

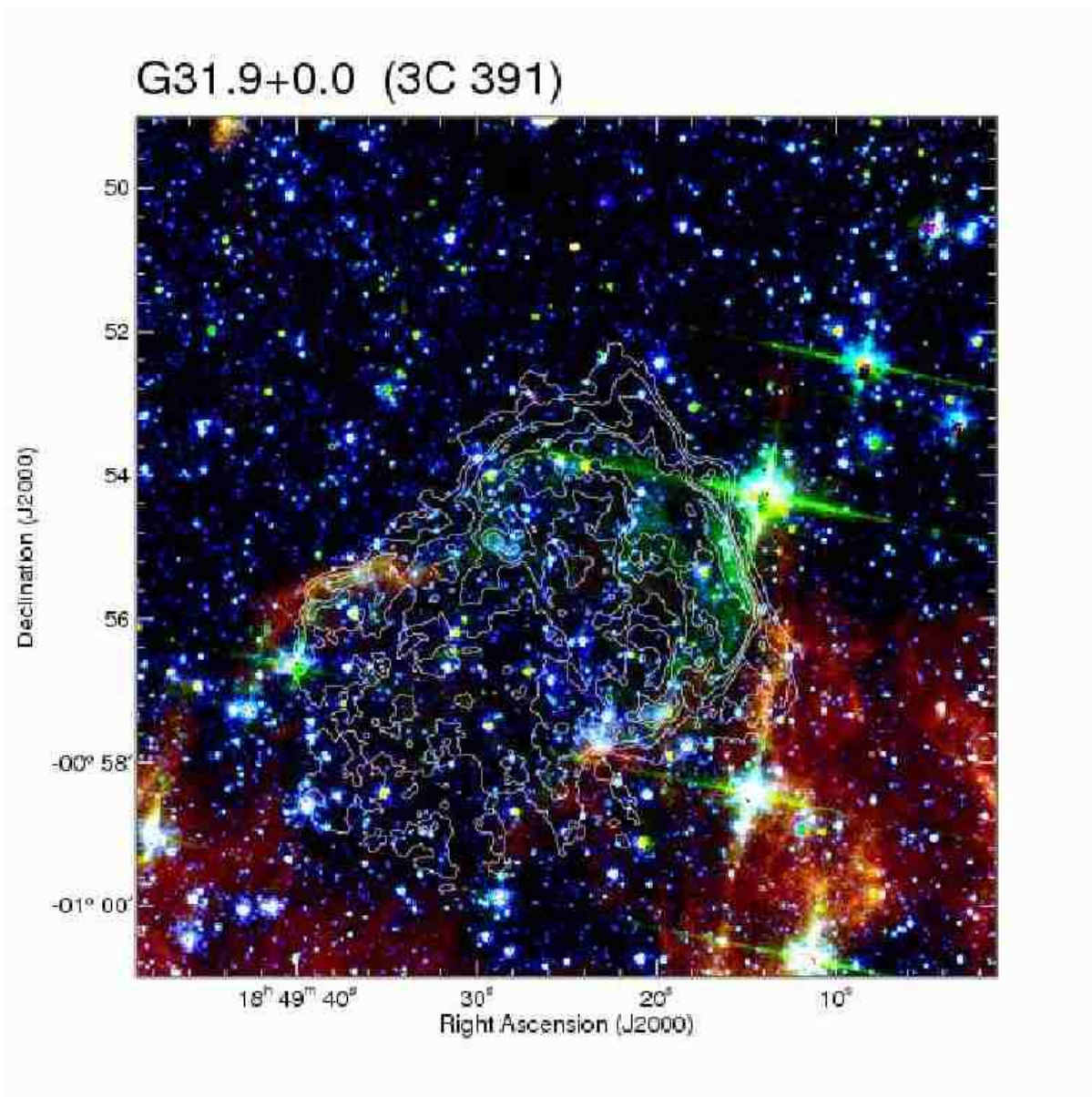


Fig. 9.— G31.9+0.0 (3C 391) R (8.0 μm), G (5.8 μm), B (4.5 μm) color image with VLA 1.46 GHz continuum map superposed. Color ranges and contour levels are the same as Fig. 1.

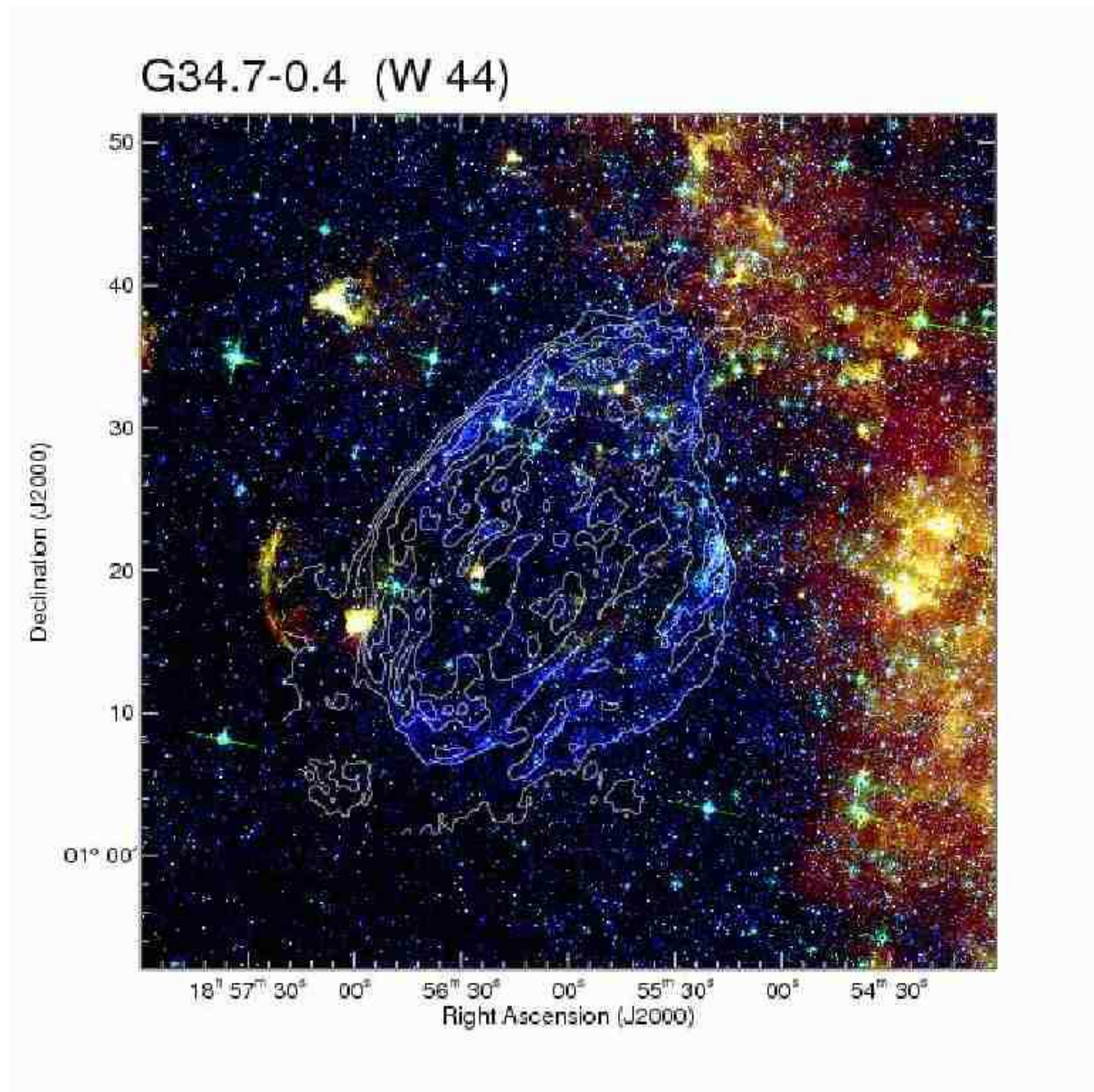


Fig. 10.— G34.7-0.4 (W 44) R (8.0 μm), G (5.8 μm), B (4.5 μm) color image with VLA 1.44 GHz continuum map superposed. Color ranges and contour levels are the same as Fig. 2.

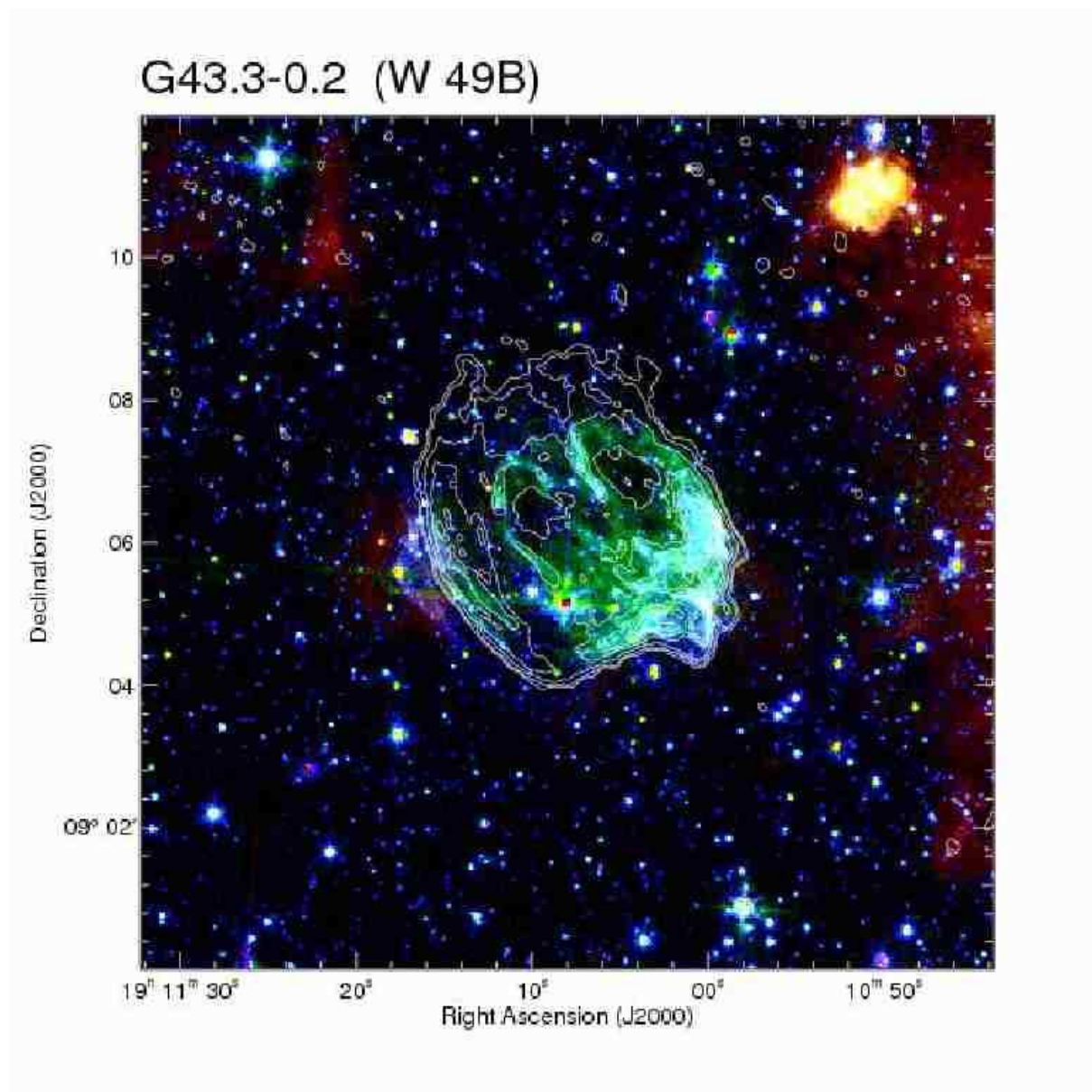


Fig. 11.— G43.3-0.2l(W 49B) R (8.0 μm), G (5.8 μm), B (4.5 μm) color image with VLA 1.45 GHz continuum map superposed. Color ranges and contour levels are the same as Fig. 3.

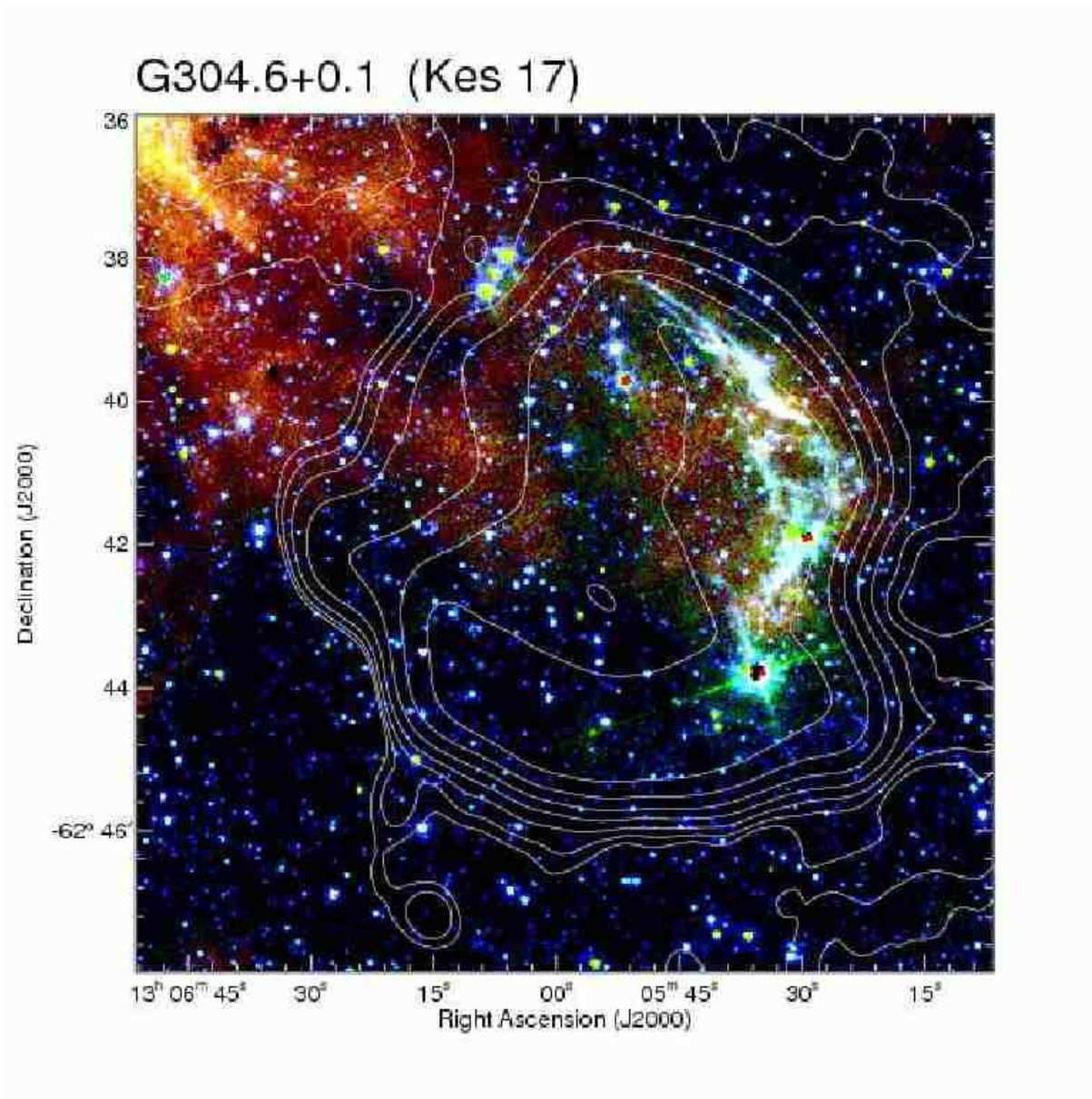


Fig. 12.— G304.6+0.1 (Kes 17) R (8.0 μm), G (5.8 μm), B (4.5 μm) color image with MOST 0.843 GHz continuum map superposed. Color ranges and contour levels are the same as Fig. 4.

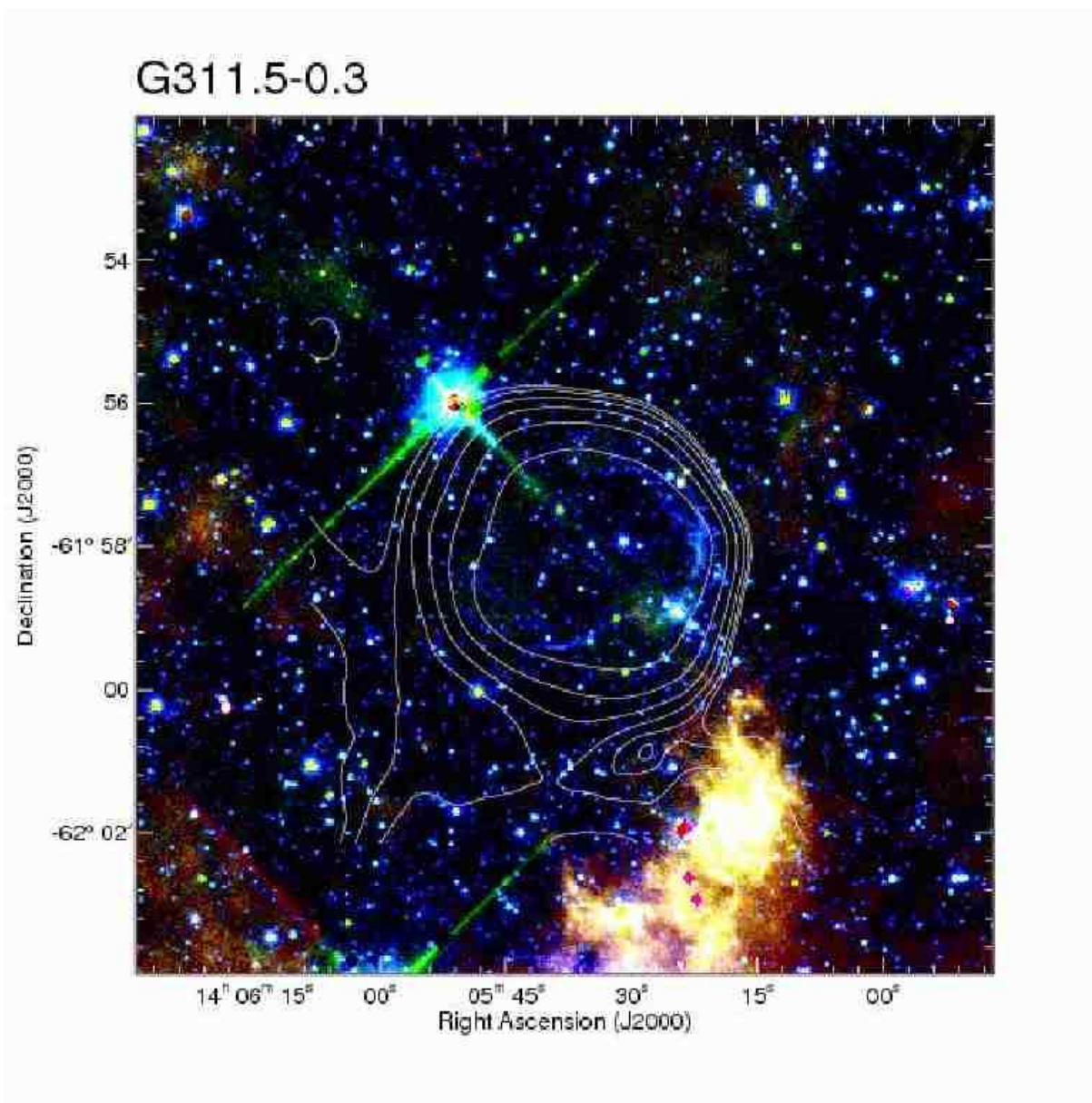


Fig. 13.— G311.5–0.3 R ($8.0\ \mu\text{m}$), G ($5.8\ \mu\text{m}$), B ($4.5\ \mu\text{m}$) color image with MOST 0.843 GHz continuum map superposed. Color ranges and contour levels are the same as Fig. 5.

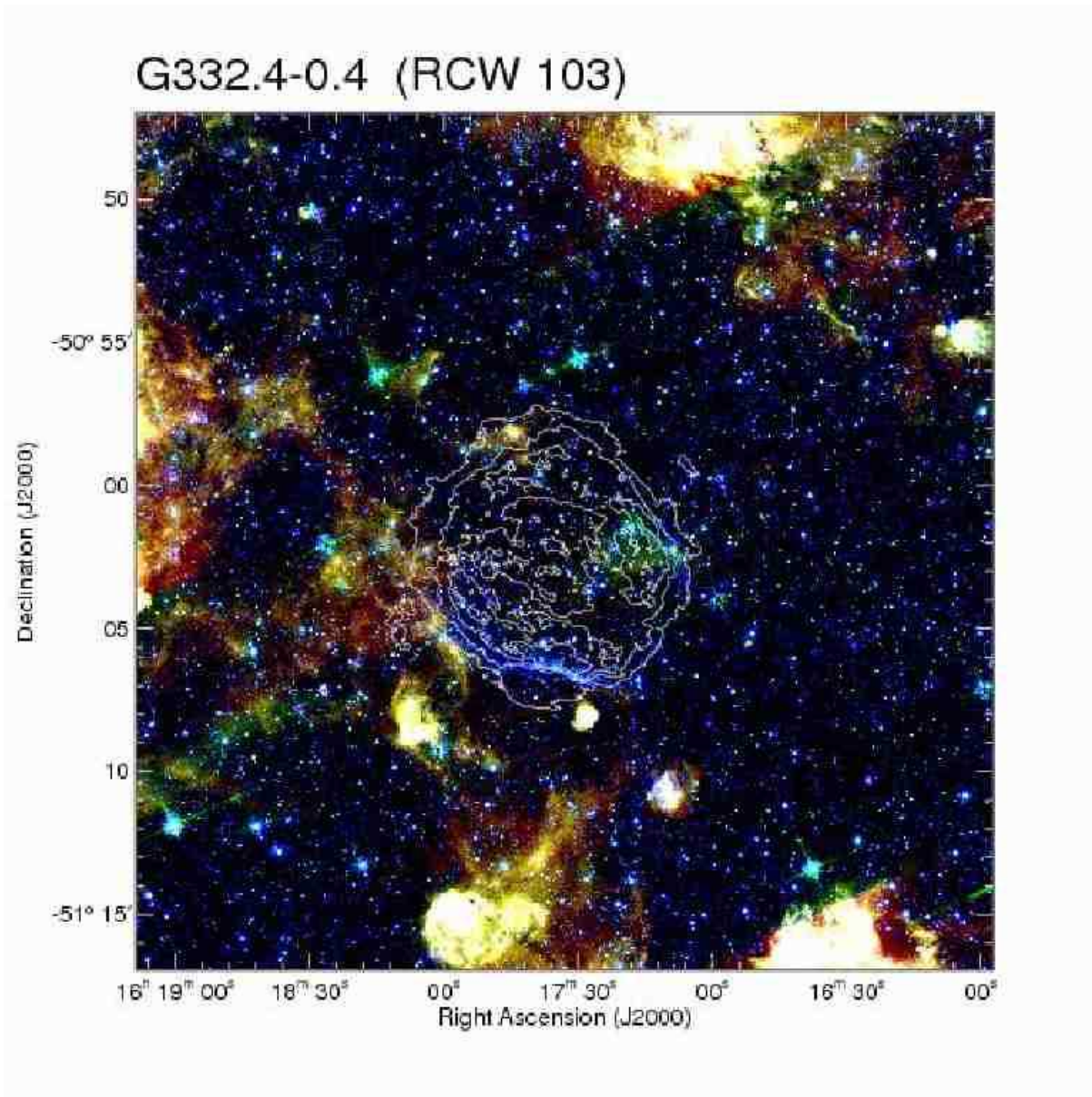


Fig. 14.— G332.4-0.4 (RCW 103) R ($8.0\ \mu\text{m}$), G ($5.8\ \mu\text{m}$), B ($4.5\ \mu\text{m}$) color image with ATCA 2.32 GHz continuum map superposed. Color ranges and contour levels are the same as Fig. 6.

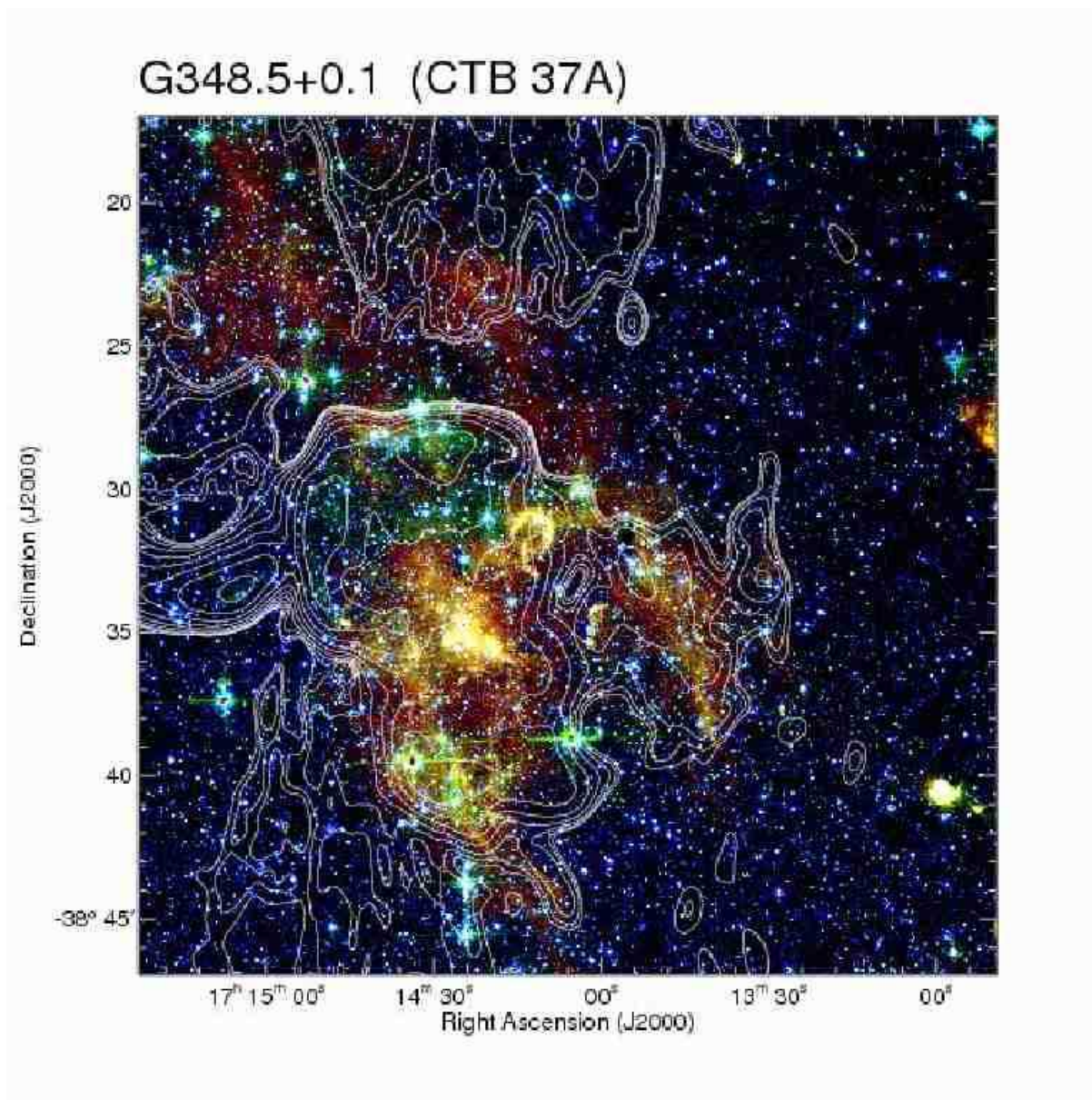


Fig. 15.— G348.5+0.1 (CTB 37A) R ($8.0\ \mu\text{m}$), G ($5.8\ \mu\text{m}$), B ($4.5\ \mu\text{m}$) color image with MOST 0.843 GHz continuum map superposed. Color ranges and contour levels are the same as Fig. 7.

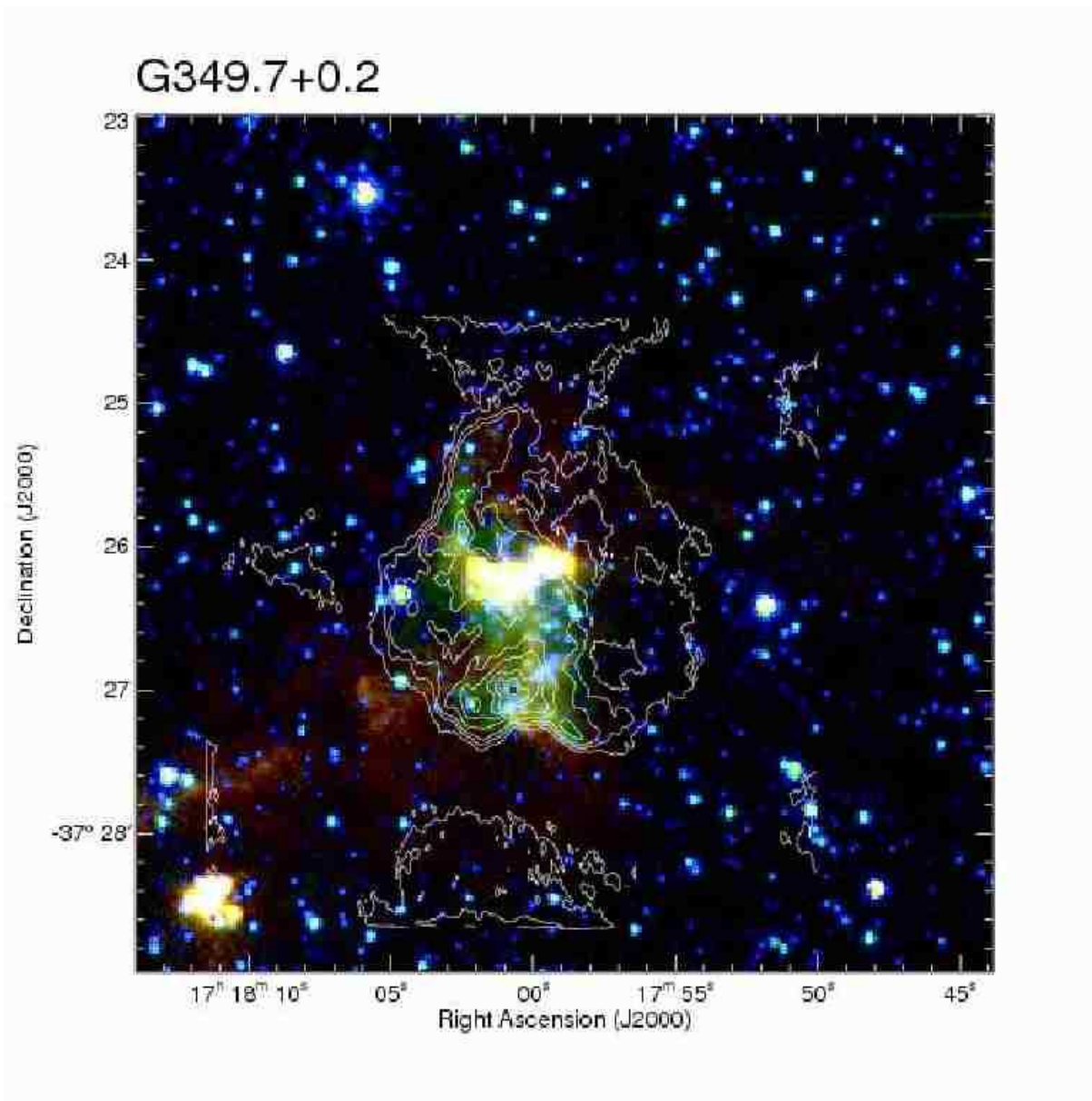


Fig. 16.— G349.7+0.2 R (8.0 μm), G (5.8 μm), B (4.5 μm) color image with VLA 1.51 GHz continuum map superposed. Color ranges and contour levels are the same as Fig. 8.

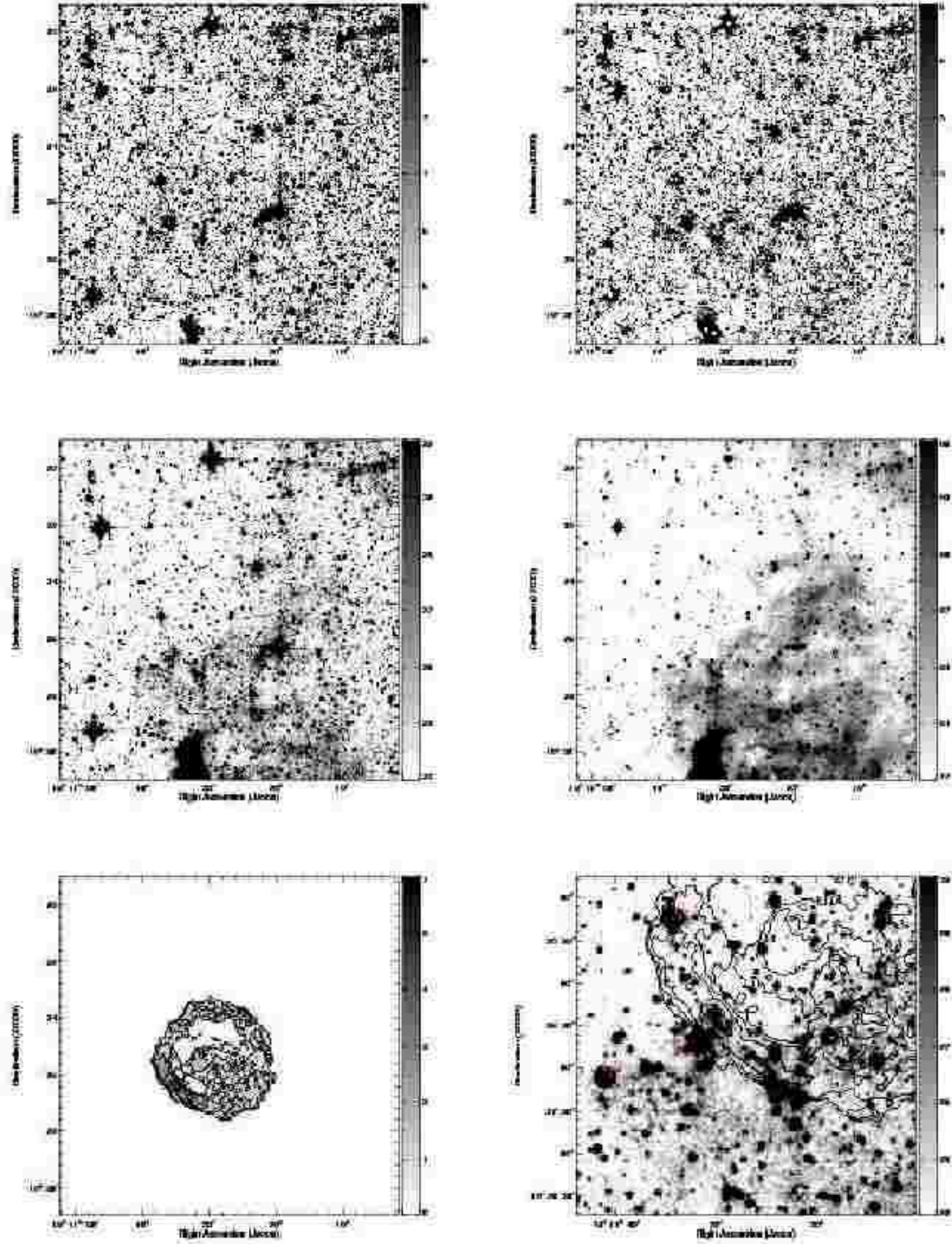


Fig. 17.— IRAC images of G11.2-0.3 at $3.6\ \mu\text{m}$ (top-left), $4.5\ \mu\text{m}$ (top-right), $5.8\ \mu\text{m}$ (middle-left), and $8.0\ \mu\text{m}$ (middle-right). The gray-scale range is shown at the left of each image. VLA 4.76 GHz continuum image with $3''.0 \times 3''.0$ beam (Green et al. 1988) is also shown at the bottom-left. The contour levels are 50, 100, 200, and 400 mJy beam^{-1} . IRAC $5.8\ \mu\text{m}$ zoom up image of infrared emission with VLA 4.76 GHz continuum contour is shown at bottom-right.

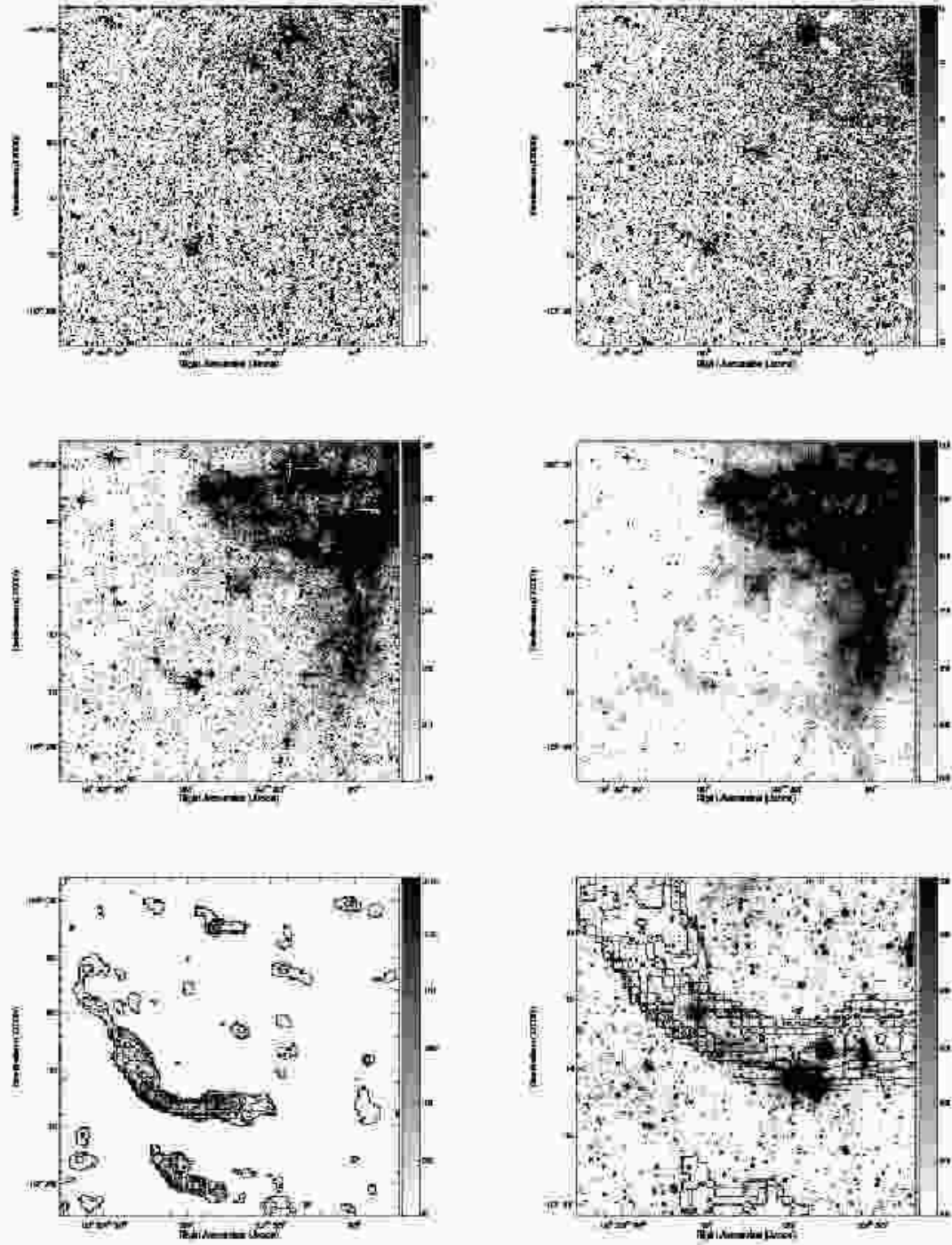


Fig. 18.— IRAC images of G21.8-0.6 (Kes 69) at $3.6\ \mu\text{m}$ (top-left), $4.5\ \mu\text{m}$ (top-right), $5.8\ \mu\text{m}$ (middle-left), and $8.0\ \mu\text{m}$ (middle-right). The gray-scale range is shown at the left of each image. NVSS 1.4 GHz continuum image with $45''.0 \times 45''.0$ beam is also shown at the bottom-left. The contour levels are 5, 10, 20, 40, 80, and $160\ \text{mJy beam}^{-1}$. IRAC $5.8\ \mu\text{m}$ zoom up image of infrared emission with NVSS 1.4 GHz continuum contour is shown at bottom-right.

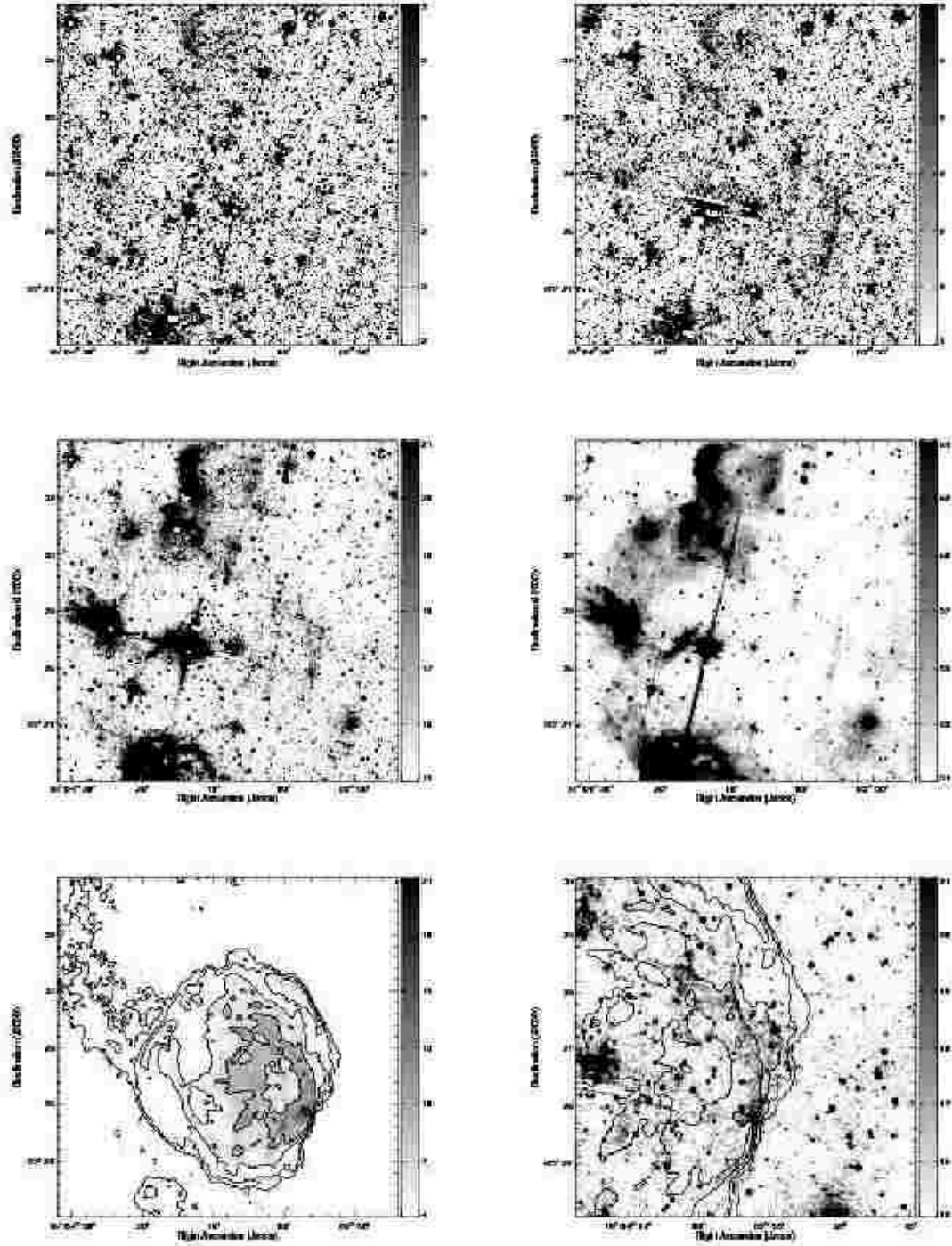


Fig. 19.— IRAC images of G39.2–0.3 (3C 396) at $3.6\ \mu\text{m}$ (top-left), $4.5\ \mu\text{m}$ (top-right), $5.8\ \mu\text{m}$ (middle-left), and $8.0\ \mu\text{m}$ (middle-right). The gray-scale range is shown at the left of each image. VLA 1.47 GHz continuum image with $6''.8 \times 6''.1$ beam (Dyer & Reynolds (1999a)) is also shown at the bottom-left. The contour levels are 1, 2, 4, 8, and 16 mJy beam^{-1} . IRAC $5.8\ \mu\text{m}$ zoom up image of infrared emission with VLA 1.47 GHz continuum contour is shown at bottom-right.

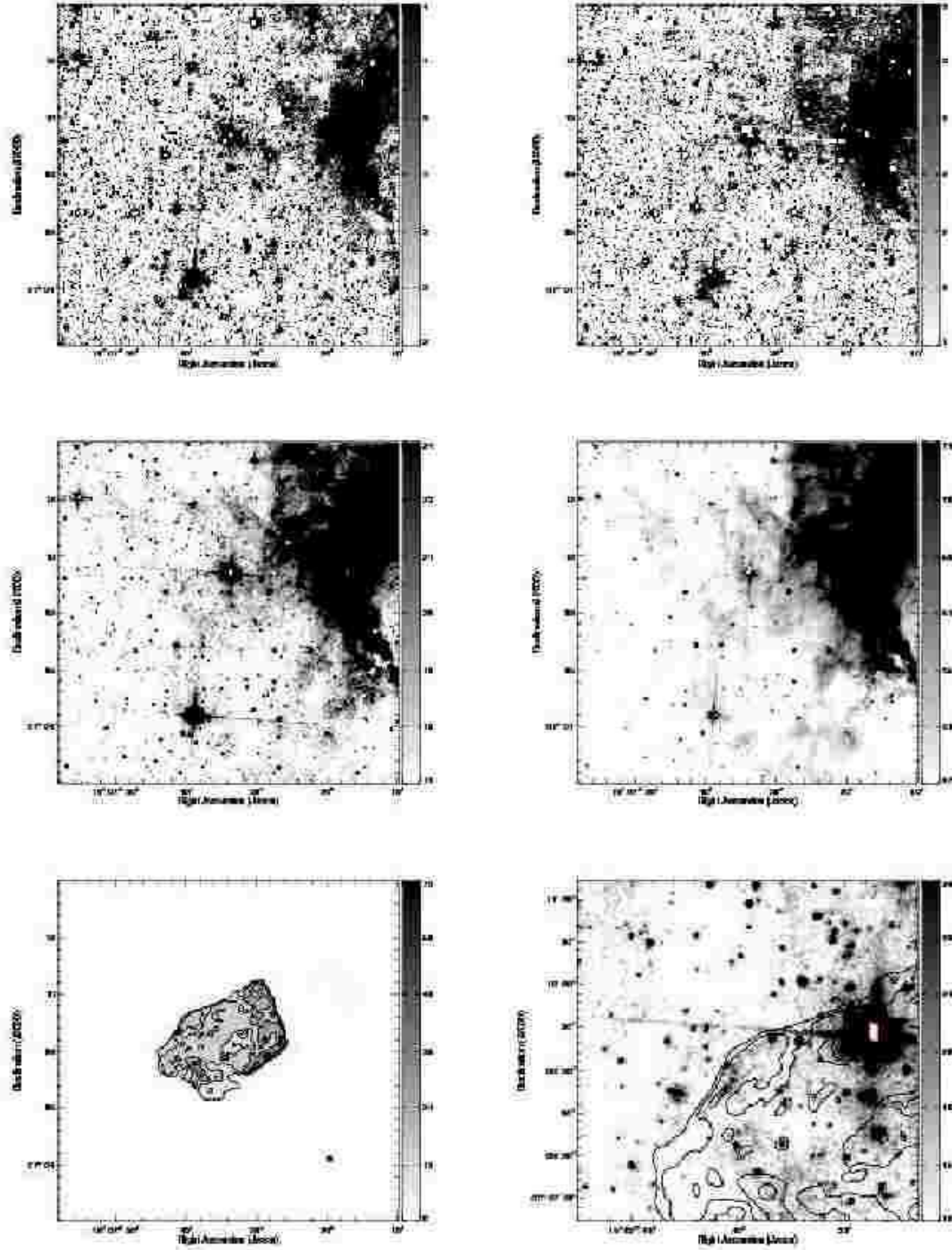


Fig. 20.— IRAC images of G41.1–0.3 (3C 397) at $3.6\ \mu\text{m}$ (top-left), $4.5\ \mu\text{m}$ (top-right), $5.8\ \mu\text{m}$ (middle-left), and $8.0\ \mu\text{m}$ (middle-right). The gray-scale range is shown at the left of each image. VLA $1.47\ \text{GHz}$ continuum image with $6''.4 \times 6''.1$ beam (Dyer & Reynolds (1999b)) is also shown at the bottom-left. The contour levels are 5, 10, 20, 40, and $80\ \text{mJy beam}^{-1}$. IRAC $5.8\ \mu\text{m}$ zoom up image of infrared emission with VLA $1.47\ \text{GHz}$ continuum contour is shown at bottom-right.

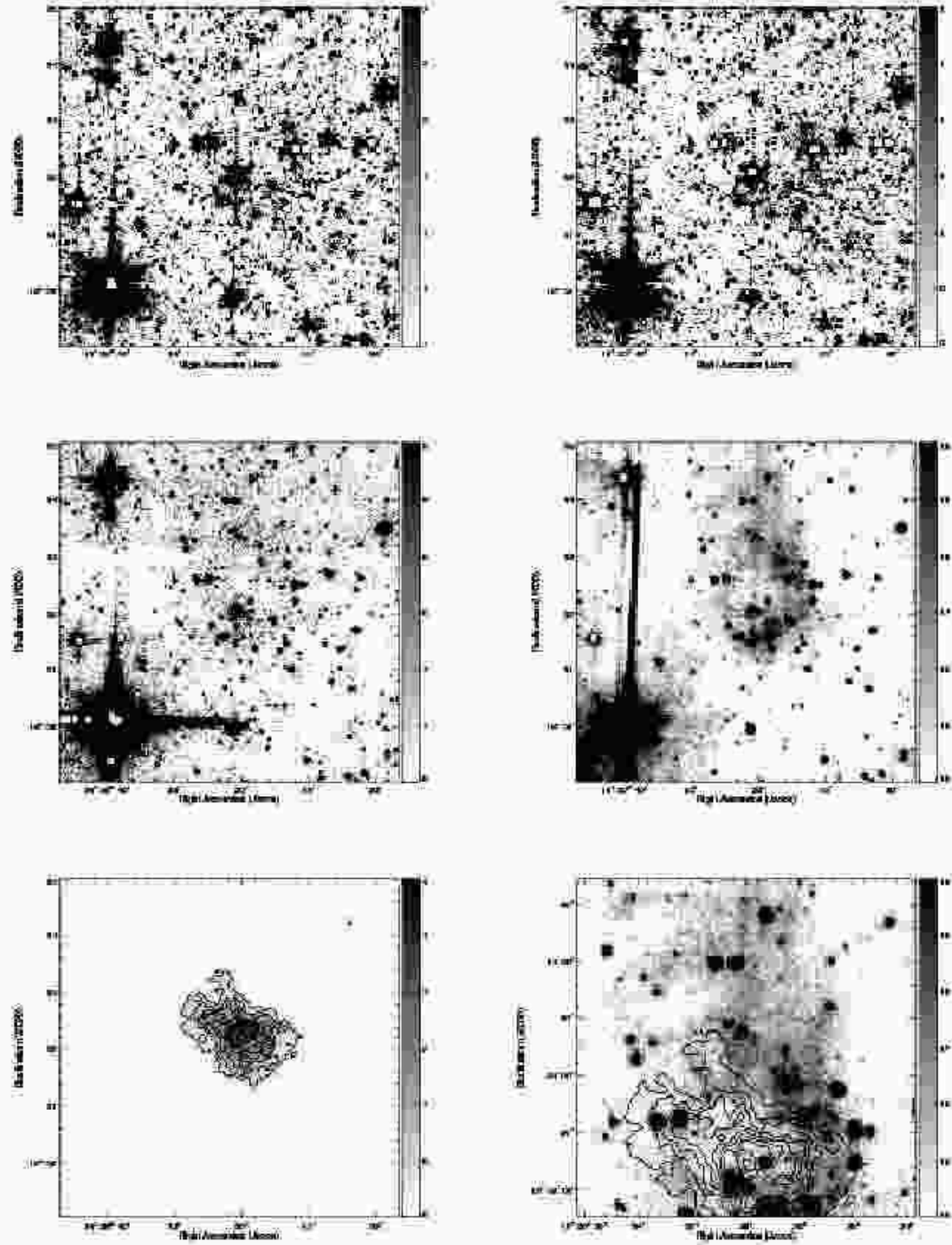


Fig. 21.— IRAC images of G54.1+0.3 at $3.6\ \mu\text{m}$ (top-left), $4.5\ \mu\text{m}$ (top-right), $5.8\ \mu\text{m}$ (middle-left), and $8.0\ \mu\text{m}$ (middle-right). The gray-scale range is shown at the left of each image. VLA 4.85 GHz continuum image with $6''.2 \times 5''.2$ beam is also shown at the bottom-left. The contour levels are 5, 10, 20, 40, 80, and $160\ \text{mJy beam}^{-1}$. IRAC $8.0\ \mu\text{m}$ zoom up image of infrared emission with VLA 4.85 GHz continuum contour is shown at bottom-right.

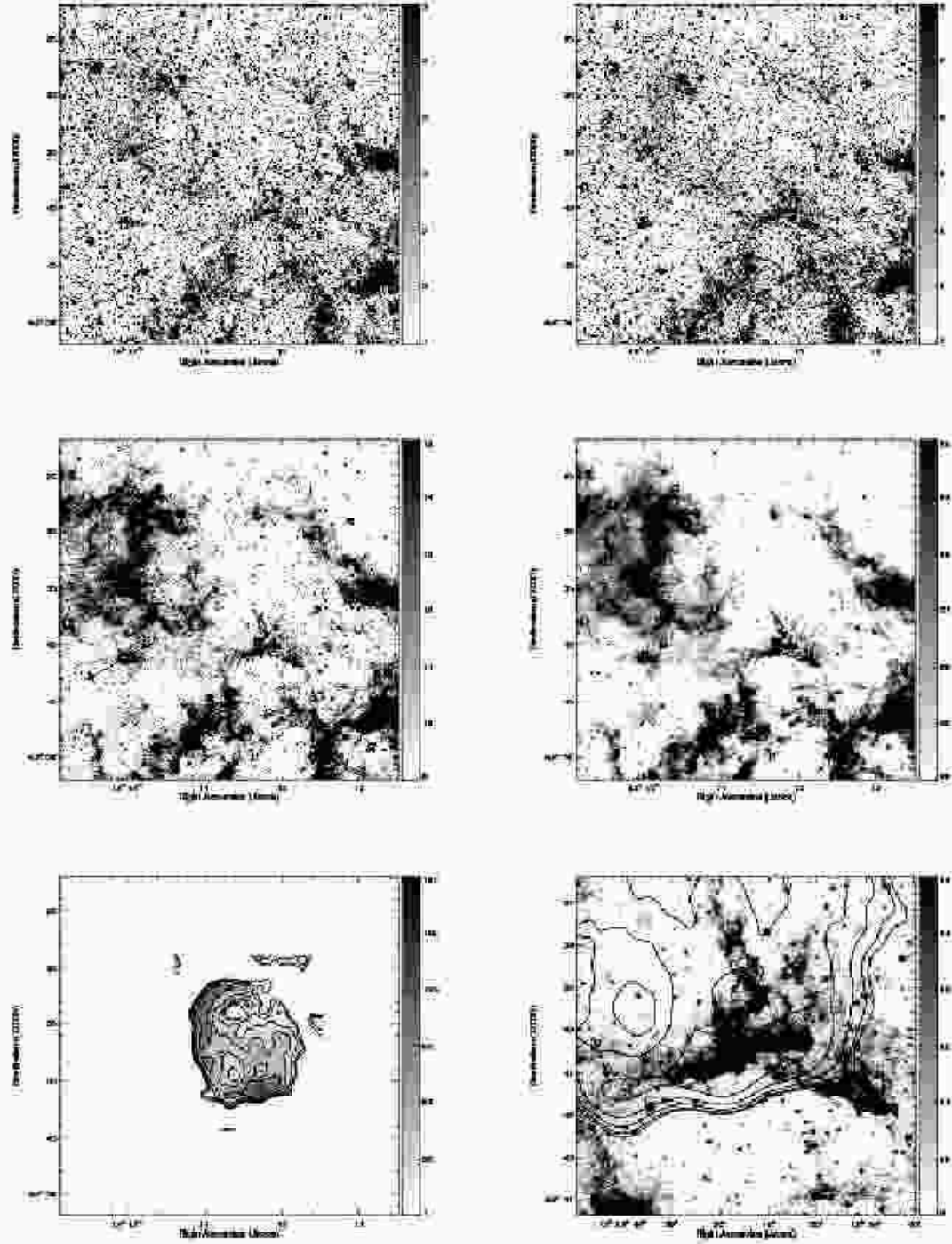


Fig. 22.— IRAC images of G298.6–0.0 at $3.6\ \mu\text{m}$ (top-left), $4.5\ \mu\text{m}$ (top-right), $5.8\ \mu\text{m}$ (middle-left), and $8.0\ \mu\text{m}$ (middle-right). The gray-scale range is shown at the left of each image. MOST 0.843 GHz continuum image with $43'' \times 43''$ beam is also shown at the bottom-left. The contour levels are 5, 10, 20, 40, 80, and $160\ \text{mJy beam}^{-1}$. IRAC $5.8\ \mu\text{m}$ zoom up image of infrared emission with MOST 0.843 GHz continuum contour is shown at bottom-right.

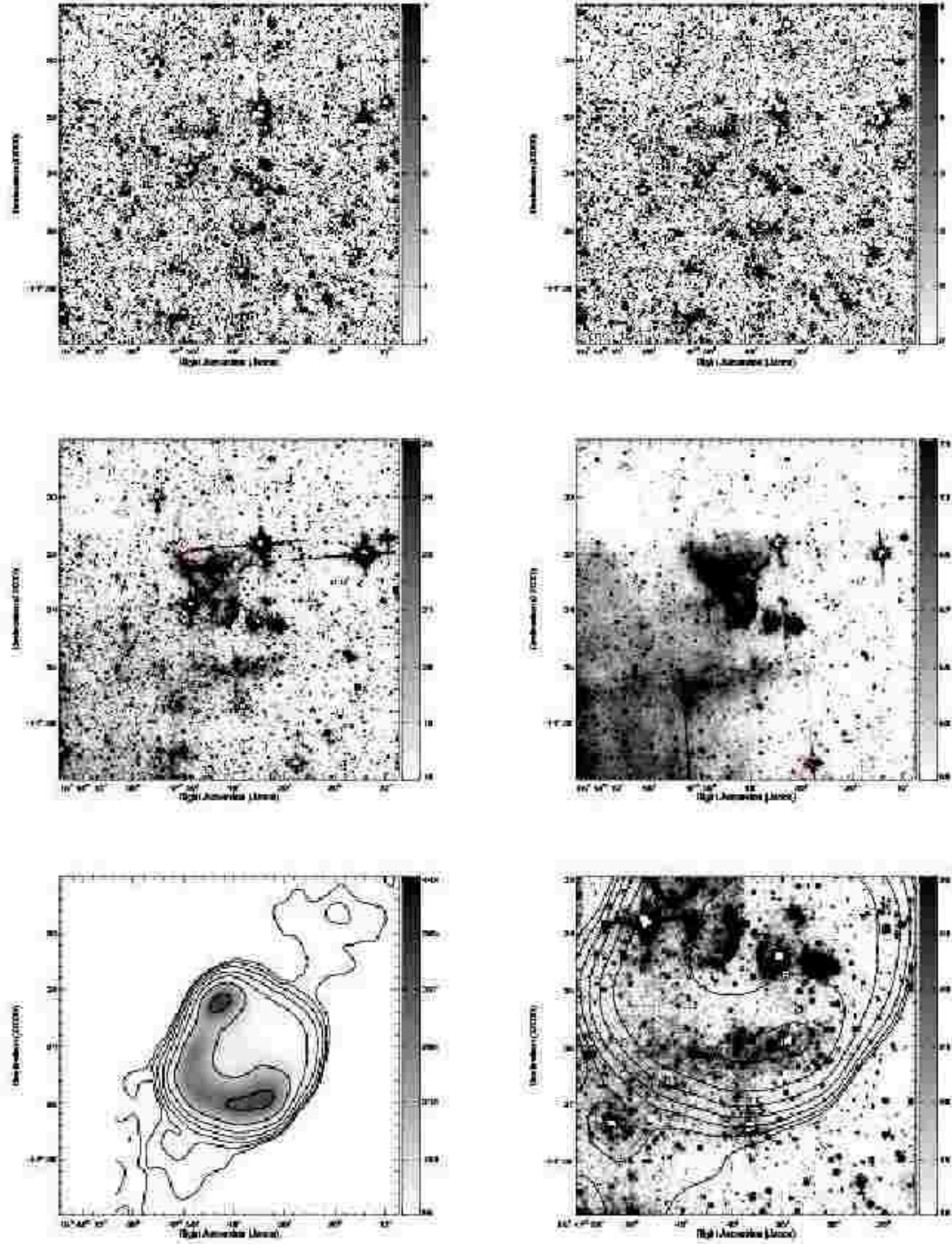


Fig. 23.— IRAC images of G340.6+0.3 at $3.6\ \mu\text{m}$ (top-left), $4.5\ \mu\text{m}$ (top-right), $5.8\ \mu\text{m}$ (middle-left), and $8.0\ \mu\text{m}$ (middle-right). The gray-scale range is shown at the left of each image. MOST 0.843 GHz continuum image with $43'' \times 43''$ beam is also shown at the bottom-left. The contour levels are 5, 10, 20, 40, 80, 160, and $320\ \text{mJy beam}^{-1}$. IRAC $5.8\ \mu\text{m}$ zoom up image of infrared emission with MOST 0.843 GHz continuum contour is shown at bottom-right.

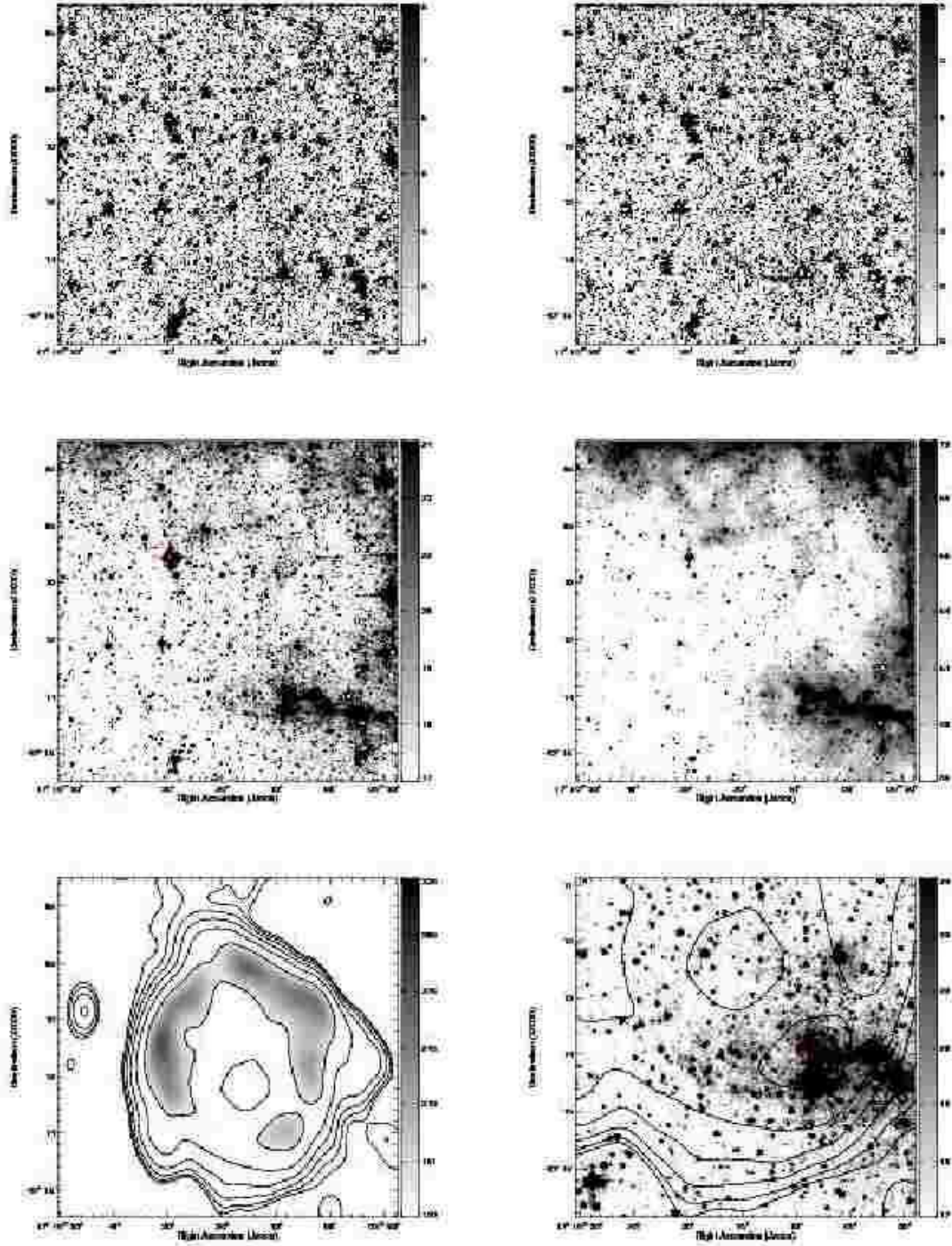


Fig. 24.— IRAC images of G346.6–0.2 at $3.6\ \mu\text{m}$ (top-left), $4.5\ \mu\text{m}$ (top-right), $5.8\ \mu\text{m}$ (middle-left), and $8.0\ \mu\text{m}$ (middle-right). The gray-scale range is shown at the left of each image. MOST 0.843 GHz continuum image with $43'' \times 43''$ beam is also shown at the bottom-left. The contour levels are 5, 10, 20, 40, 80, and $160\ \text{mJy beam}^{-1}$. IRAC $5.8\ \mu\text{m}$ zoom up image of infrared emission with MOST 0.843 GHz continuum contour is shown at bottom-right.